Crystal ribcage: a platform for probing real-time lung function at cellular resolution in health and disease

Authors: Rohin Banerji[1]†, Gabrielle N. Grifno[1]†, Linzheng Shi[1], Dylan Smolen[1], Rob LeBourdais[1], Johnathan Muhvich[1], Cate Eberman[1], Bradley E. Hiller[2], Jisu Lee[2], Kathryn Regan[1], Siyi Zheng[1], Sue Zhang[1], John Jiang[1], Ahmed A. Raslan[2,3], Julia C. Breda[4], Riley Pihl[2], Katrina Traber[2], Sarah Mazzilli[4], Giovanni Ligresti[2], Joseph P. Mizgerd[2], Béla Suki[1], Hadi T. Nia[1,2*]

Affiliations:
[1] Department of Biomedical Engineering, Boston University; Boston MA
[2] Pulmonary Center, Boston University Chobanian & Avedisian School of Medicine; Boston MA
[3] Department of Zoology, Faculty of Science, Assiut University; Assiut Egypt
[4] Section of Computational Biomedicine, Boston University Chobanian & Avedisian School of Medicine; Boston MA
† These authors contributed equally to this work
[*] Corresponding author. Email: htnia@bu.edu

Abstract

Understanding the dynamic pathogenesis and treatment response in pulmonary diseases requires probing the lung at cellular resolution in real-time. Despite recent progress in intravital imaging, optical imaging of the lung during active respiration and circulation has remained challenging. Here, we introduce the crystal ribcage: a transparent ribcage that (i) allows truly multiscale optical imaging of the lung in health and disease from whole-organ to single cell, (ii) enables the modulation of lung biophysics and immunity through intravascular, intrapulmonary, intraparenchymal, and optogenetic interventions, and (iii) preserves the 3-D architecture, air-liquid interface, cellular diversity, and respiratory-circulatory functions of the lung. Utilizing these unprecedented capabilities on murine models of primary and metastatic lung tumors, respiratory infection, pulmonary fibrosis, emphysema, and acute lung injury we probed how disease progression remodels the respiratory-circulatory functions at the single alveolus and capillary levels. In cancer, we identified the earliest stage of tumorigenesis that compromises alveolar and capillary functions, a key state with consequences on tumor progression and treatment response. In pneumonia, we mapped mutual links between the recruited immune cells and the alveolar-capillary functions. We found that neutrophil migration is strongly and reversibly responsive to vascular pressure with implications for understanding of how lung physiology, altered by disease and anatomical location, affects immune cell activities. The crystal ribcage and its broad applications presented here will facilitate further studies of real-time remodeling of the alveoli and capillaries during pathogenesis of nearly any pulmonary disease, leading to the identification of new targets for treatment strategies.

Introduction

The lung is continuously exposed to mechanical, biological, and immunological stresses and is the site of many fatal pathologies such as primary and metastatic cancers, respiratory infections, and both obstructive and restrictive diseases. Our limited understanding of lung pathophysiology was

exemplified by the COVID-19 pandemic. Mechanistic understanding of the complex structure-function of the lung at the cellular level and its remodeling at the earliest stages of disease requires characterization of cause-effect relationships at multiple scales down to cellular resolution.

Enclosed by the ribcage and continuously in motion, the functioning lung is a challenging organ to study in real-time at cellular resolution. Clinical imaging modalities (e.g., MRI, CT, and PET) cannot spatiotemporally resolve dynamic alveolar function, capillary flow, and cellular trafficking and motility during respiration. Histological analyses are "snapshot" images of fixed lungs at subcellular resolution without temporal dynamics of the lung microphysiology. Intravital microscopy recently enabled high resolution imaging of microcirculation in real-time[1-5], which led to major discoveries in lung biology and immunity[2,5-7]. However, these methods (i) compromise the respiratory function of the lung, a defining feature of the pulmonary system with crucial effects on the physics, biology, and immunity of the lung[8-11], and (ii) can only visualize limited alveoli of the lung through a small imaging window, unable to capture whole-organ heterogeneities or track rare and dynamic events that may span beyond the imaging window.

In a major departure from existing approaches, we introduce the crystal ribcage – a transparent ribcage that enables optical imaging of nearly the entire surface of a functioning mouse lung in real-time and at cellular resolution with preserved respiratory and circulatory functions. We combine *in vivo* benefits – preserved cellular diversity and complex lung architecture – with organ-on-chip model capabilities – optical imaging and high controllability of microphysiology – in the crystal ribcage to perturb the biophysics and immunity of the lung through intrapulmonary, intravascular, and optogenetic interventions while visualizing real-time cellular events. This provides enormous opportunities for understanding cause-effect relationships in the pathogenesis of pulmonary diseases. We utilized the crystal ribcage to probe remodeling of alveolar and capillary functions in mouse models of primary and metastatic lung cancer, bacterial infection, pulmonary fibrosis, emphysema, and acute lung injury. We identified the earliest stage of tumorigenesis when alveolar structure-functions are compromised, probed the dynamic circulatory functions of capillaries remodeled by tumor growth and pneumonia, and demonstrated a dramatic and reversible mechano-responsiveness in immune cell migration in the lung.

Results

Crystal ribcage: Development, validation, and capabilities

The crystal ribcage is a transparent, biocompatible platform designed to provide a physiological environment for a functioning lung *ex vivo* that enables truly multiscale optical imaging of the lung in health and disease. The crystal ribcage allows 3-D imaging over the entire surface of the lung (**Fig. 1a**), while uniquely combining the benefits of *in vivo* mouse models (cellular diversity, 3-D lung architecture, breathing and circulation) and *in vitro* organ-on-chip models[12] (imaging advantages and extensive, precise control over microphysiology) (**Fig. 1b**). We designed the crystal ribcage to mimic the geometry and surface properties of the native ribcage to preserve the *in vivo* physiological conditions of the mouse lung during imaging. Using micro computed tomography (μCT) data of mouse chest cavities, we created 3-D molds of the ribcage that were age and strain specific for mice of interest (in this study: C57/B6, FVB N/J and A/J strains, aged 6-12 weeks). The mold was used in multi-step additive, sacrificial, and thermoforming processes to fabricate the crystal ribcage (**Fig. 1c**, **Extended Data Fig. 1**). We engineered the internal crystal ribcage surface to be hydrophilic, mimicking the native parietal pleura in the mouse chest, so that the lung slides freely along it in its natural configuration (**Supplemental Fig. 1a, Supplemental Video 1-4**). We fabricated the crystal ribcage to be 150 μm thick for imaging with high-powered objectives (e.g., 60x), and confirmed that the ribcage geometry did not cause optical aberrations (**Supplemental Fig. 1b,c**). We fabricated rigid and semi-rigid versions of crystal ribcage using polystyrene and polydimethylsiloxane (PDMS), respectively. Both materials are biocompatible, free of autofluorescence and ubiquitous in biological research. The rigid crystal ribcage allows positive- and negative-pressure ventilation as in mechanically assisted or spontaneous breathing, respectively (**Supplemental Video 1**). The rigid crystal ribcage closely mimics the *in vivo* ribcage in quiet breathing as the majority of the lung deformation is achieved by the diaphragm[13] (also see **Extended Data Fig. 2a,b**). The semi-deformable PDMS ribcage mimics the macroscale ribcage deformation that occurs during *in vivo* events such as exercise, sighs, and coughs. The PDMS ribcage is also pierceable and self-healing to enable intraparenchymal injections. Finally, we confirmed that the crystal ribcage does not affect alveolar respiratory function by directly comparing ventilation inside the crystal ribcage to ventilation inside the intact mouse ribcage (**Extended Data Fig. 2c**).

The crystal ribcage is equipped with custom and commercial ventilators for negative- and positive-pressure ventilation, both uniform and pulsatile perfusion pumps, and sensors with a data acquisition unit to preserve and assess the lung's circulatory and respiratory functions (**Fig. 1d**). The crystal ribcage is attached to a custom 6-degree-of-freedom arm to position any region of the lung surface on top of or under a microscope to image the whole lobe or single alveoli using any optical imaging modality (**Fig. 1e, Extended Data Fig. 3**). This allows probing anatomically localized pulmonary diseases, such as lobar pneumonia (**Fig. 1e**) and capturing sporadic features such as tumor metastases (**Fig. 1f)**.

We quantified alveolar respiratory function by imaging a specific region of interest (ROI) on the lung surface over the normal inspiratory quasi-static pressure range from 3 to 18 cmH_2O[14] (**Fig. 1g**). We then computed the sub-alveolar strain (normalized deformation) field (**Fig. 1h**) over this pressure range, as an indirect measure of alveolar functionality. Next, we studied alveolar

mechanics during dynamic positive-pressure ventilation at 120 and 60 breaths/min while maintaining a positive end expiratory pressure (PEEP) of 4 cmH_2O and a peak inspiratory pressure (PIP) of 12-14 cmH_2O (**Fig. 1i, Extended Data Fig. 4**). We found that alveoli near the base of the lung have a larger diameter for a longer duration of the ventilation cycle at higher respiratory rates (120 breaths/min).

We next probed pulmonary circulation in the context of cancer and other pathologies using the crystal ribcage. First, we imaged the spatiotemporal dynamics of a fluorescent dye distribution (**Fig. 1j**). Second, we imaged single capillary and trafficking of single immune cell within the capillary at high spatiotemporal resolution (**Fig. 1k, Supplemental Fig. 2, Supplemental Video 5**). The crystal ribcage simultaneously enables imaging of key resident cell types in the lung, as demonstrated for alveolar type II cells (SPC-GFP+; **Extended Data Fig. 5**) and can be used to visualize the lung illuminated with fluorescent nuclear, membrane, and vascular labels, or through label-free approaches such as second harmonic generation (SHG).

We demonstrated the versatility of the crystal ribcage to probe lung dysfunction in nearly any pulmonary disease or condition with parenchymal presentation (**Fig. 1l**), such as primary and metastatic breast cancer (**Fig. 2**), pneumonia and acute injury (**Fig. 3-5**), emphysema, and fibrosis (**Supplemental Figs. 2,3)** at the whole organ, whole lobe, and alveolar scales.

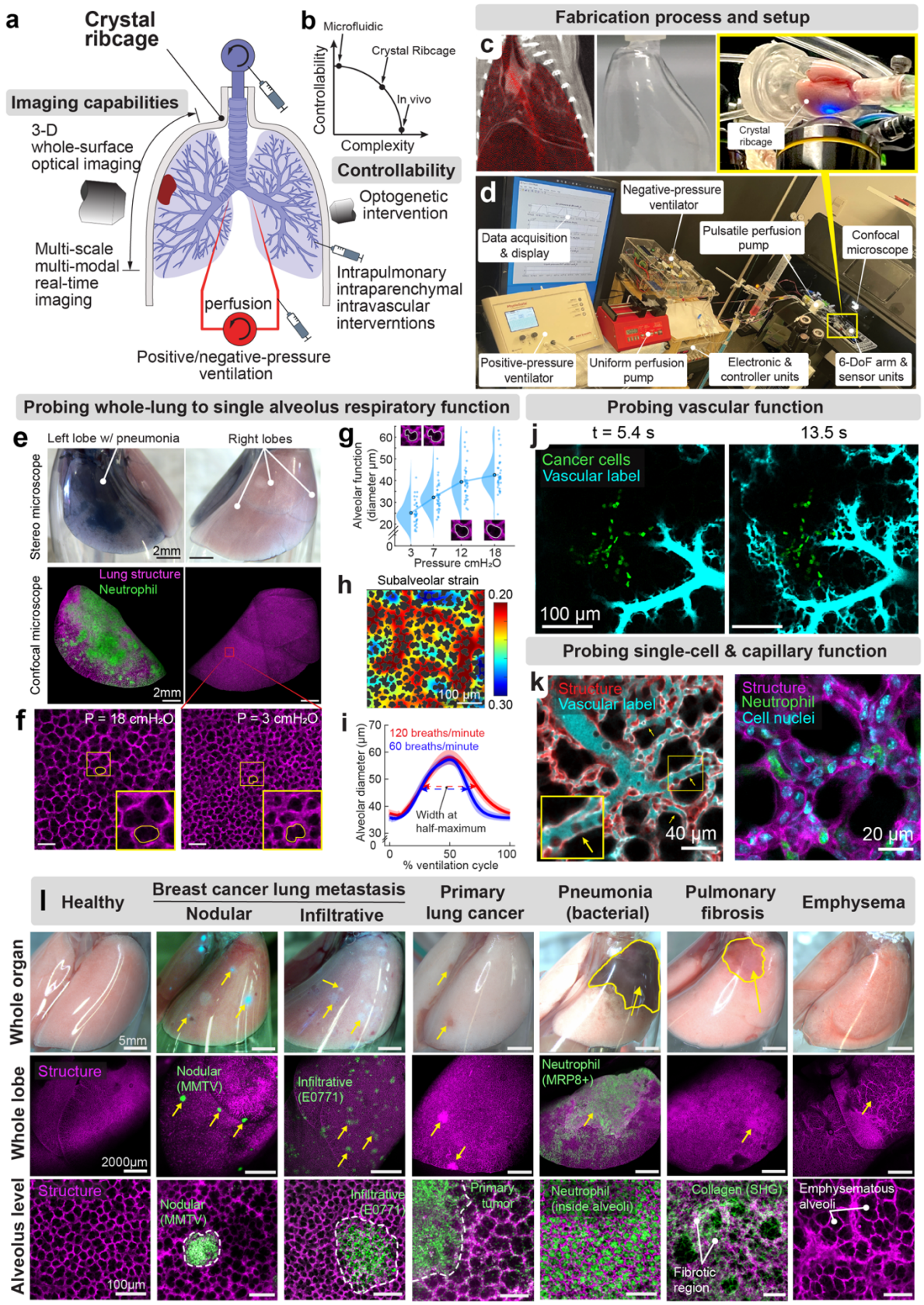
a
Crystal ribcage
Imaging capabilities
3-D whole-surface optical imaging
Multi-scale multi-modal real-time imaging
perfusion
Positive/negative-pressure ventilation
Intrapulmonary intraparenchymal intravascular interverntions
Optogenetic intervention
Controllability
b
Microfluidic
Crystal Ribcage
In vivo
Controllability
Complexity
Fabrication process and setup
c
Crystal ribcage
d
Negative-pressure ventilator
Data acquisition & display
Pulsatile perfusion pump
Confocal microscope
Positive-pressure ventilator
Uniform perfusion pump
Electronic & controller units
6-DoF arm & sensor units
Probing whole-lung to single alveolus respiratory function
e
Left lobe w/ pneumonia
Right lobes
Stereo microscope
2mm
Confocal microscope
Lung structure
Neutrophil
2mm
f
P = 18 cmH₂O
P = 3 cmH₂O
g
Alveolar function (diameter µm)
Pressure cmH₂O
h
Subalveolar strain
0.20
0.30
100 µm
i
120 breaths/minute
60 breaths/minute
Alveolar diameter (µm)
Width at half-maximum
% ventilation cycle
Probing vascular function
j
t = 5.4 s
13.5 s
Cancer cells
Vascular label
100 µm
Probing single-cell & capillary function
k
Structure
Vascular label
40 µm
Structure
Neutrophil
Cell nuclei
20 µm
l
Healthy
Breast cancer lung metastasis
Nodular
Infiltrative
Primary lung cancer
Pneumonia (bacterial)
Pulmonary fibrosis
Emphysema
Whole organ
5mm
Whole lobe
Structure
2000µm
Nodular (MMTV)
Infiltrative (E0771)
Neutrophil (MRP8+)
Alveolus level
Structure
100µm
Nodular (MMTV)
Infiltrative (E0771)
Primary tumor
Neutrophil (inside alveoli)
Collagen (SHG)
Fibrotic region
Emphysematous alveoli

137

FIGURE 1 | Development, capabilities, and application of the crystal ribcage in pulmonary research. (a) Schematic representation of imaging, controllability, and intervention capabilities of the crystal ribcage. **(b)** The crystal ribcage benefits from the imaging capabilities and controllability of organ-on-chip models while preserving the complexities and cellular diversity of *in vivo* lungs. **(c)** Age- and strain-specific μCT scans used to model the mouse chest cavity to fabricate the crystal ribcage through a multistep additive and sacrificial fabrication process. **(d)** The portable platform to maintain, monitor, and record the lung physiological condition during real-time imaging. **(e)** Imaging the distal lung surface with preserved 3-D geometry, demonstrated by both stereo- and confocal-microscopy imaging of the right and left lobes of a mouse lung with a left-lobar bacterial pneumonia infection (labeled by leakage of intravascular Evans blue into the lung airspace) showing neutrophil infiltration 24 hours after initial infection. **(f)** Imaging desired regions of the lung and tracking alveoli (contoured alveolus for reference) across the respiratory cycle under quasi-static conditions. **(g)** Alveolar function assessed by measuring alveolar diameter as a function of quasi-static alveolar air pressure. The distribution of diameters are connected by the means from m=4 ROI over n=4 mice. **(h)** Representative map of the strain experienced by the alveolar septum during quasi-static ventilation, with sub-alveolus resolution for m=1 ROI. **(i)** Alveolar diameter measured at distinct points of the ventilation cycles at 120 and 60 breaths/min presented as mean ± SEM of data from m=4 ROI over n=2 mice **(j)** Remodeling of single capillary function in lung cancer assessed by real-time confocal microscopy of the spatiotemporal distribution of a Cascade Blue-dextran (10 kDa) flow under quasi-static inflation. **(k)** Cellular activity and alveolar-capillary structure-function imaged during quasi-static inflation, inset yellow box shows a single capillary with shadow of cells inside it. (**l**) The crystal ribcage capabilities demonstrated on models of breast cancer lung metastasis, primary lung cancer, respiratory infection, pulmonary fibrosis, and emphysema from whole organ down to alveolus, capillary, and cell length and functional scales, imaged with confocal and multi-photon microscopy.

Disruption of alveolar and capillary dynamics by tumor growth

Primary lung cancer is among the leading fatal cancers [15]. The lung is also a major site of metastasis for many cancer types including breast cancer[16]. While early steps of cancer cell extravasation and immune interactions have been studied using intravital microscopy in a lung immobilized by glue or vacuum[1,3], understanding of tumor dynamics during active respiration and circulation is lacking.

To answer long-standing questions surrounding remodeling of alveolar structure and function by tumors, we investigated two mouse models of breast cancer lung metastasis with differential growth patterns. According to our previous work[17] and others[18], tumor growth patterns are generally categorized as *nodular* (cells grow as a dense nodule pushing away normal tissue) or *infiltrative* (cancer cells replace normal cells with minimal remodeling of existing tissue; also known as co-optive[18]), with distinct biological and clinical outcomes. Infiltrative tumors co-opt the tissue's existing blood vessels and structure and initiate less angiogenesis[19]. In contrast, nodular tumors disrupt existing microarchitecture and form new blood vessels[18]. We have previously characterized differential growth patterns in infiltrative primary brain tumors (e.g., glioblastoma) versus nodular metastatic brain tumors[17]. Surprisingly, the same two phenotypes were also observed in breast cancer metastasis to the lung. Next, we probed the differential remodeling of the peritumor microenvironment[20].

We modeled nodular and infiltrative metastatic tumors using murine breast cancer cell lines MCa-M3C-H2B-dendra2 and E0771-H2B-dendra2, respectively (**Fig. 2a,b**). The nodular phenotype tumors appeared to both "push" into the lung tissue and bulge out of the pleural surface of the lung, while the infiltrative phenotype appeared to replace the existing lung tissue and was located superficially on the pleural surface (**Extended Data Fig. 6a,b**). Upon probing the mechanics of local alveoli, we observed that alveoli filled with nodular tumors in the range of 100-200 μm in diameter lacked the ability to change volume (**Fig. 2a**) impairing respiratory function. These alveoli remained maximally dilated across all alveolar pressures, indicating that nodular cancer cells distend and fill the alveolar airspace. Interestingly, functional impairment extended up to 1-

2 alveoli into the peritumoral region. Larger 1-2 mm diameter nodules caused alveoli to become stretched and compacted up to 200 μm away from the tumor boundary (**Supplemental Fig. 4,5, Supplemental Video 6**). In contrast, the infiltrative tumors did not compromise alveolar respiratory function intratumorally or peritumorally (**Fig. 2b**), suggesting that they merely take over existing tissue structures. In a carcinogen-induced model of primary lung cancer, early-stage tumors presented with a nodular-like phenotype. However, the peritumoral alveoli became emphysematous, as multiple alveoli coalesced into a single large airspace near the lesions (**Fig. 2c**). These emphysema-like airspaces were almost twice as large as alveoli far from the tumor and not as responsive to quasi-static pressure changes (**Fig. 2c**). This indicates that, despite not being directly filled with cancer cells, these alveoli still had reduced functionality compared to unaffected alveoli in the same lung.

Structural remodeling of the extracellular matrix (ECM) by tumors is strongly correlated to progression and invasion of tumors[21,22]. We investigated the collagen structure surrounding nodular and infiltrative metastatic tumors using two-photon second-harmonic generation (SHG) microscopy. Established nodules remodeled the pleural collagen to become stretched in comparison to the wavy collagen structures in the healthy lung (**Fig. 2d**). These straightened fibers indicate that alveolar walls adjacent to nodular tumors are under tension, unable to expand or contract during breathing (**Supplemental Fig. 4h**), reducing local gas exchange. In contrast, collagen fibers surrounding infiltrative tumors retained the same characteristic waviness seen in healthy tissue, implying that the structure-function of the alveoli remained unaffected. We also assessed alveolar function by computing the strain in the walls of single alveoli using a deformable image registration algorithm we adapted and validated for lung microscopy (**Supplemental Fig. 6**). Reduced strain in the septal walls during quasi-static ventilation indicates reduced alveolar functionality. In comparing the strain maps between the three different tumor types, nodular metastatic breast cancer caused the most severe dysfunction followed by the primary cancer nodules in the surrounding alveoli, and infiltrative metastatic breast cancer barely impacted local alveolar strain (**Fig. 2e**).

Next, we studied bi-directional mechanical interactions between metastatic cancer cells and the lung tissue. We first found that single cancer cells sequestered at the capillaries do not impact alveolar strain, but instead experience substantial strain themselves (**Fig. 2f, Extended Data Fig. 7**) and have lower circularity at all alveolar pressures in comparison to cells located at larger vessels (**Fig. 2g**). It was previously suggested that cancer cells experiencing high, cyclic mechanical forces contribute to tumorigenesis in *in vitro*[23]. We directly show that single cancer cells within the complex 3-D vascular architecture experience deformation in response to alveolar pressure in a functional lung, similar to what we previously reported for cell-sized polyacrylamide beads of uniform stiffness[24]. We next found metastatic nodules as small as 7-10 cells in diameter (approximately the size of one alveolus) was the critical size needed to reduce local alveolar function due to remodeling by the cancer bulk[25-28] (**Fig. 2h**).

Next, based on dramatic remodeling of alveoli by nodular tumors, we investigated the remodeled intra- and peri-tumoral capillary function. We perfused a bolus of fluorescent Cascade blue dextran (10 kDa) with RPMI cell culture media (or whole blood, **Supplemental Fig. 7**) under pressure-controlled flow of 15 cmH_2O (approximate median vascular pressure at the mouse pulmonary artery[29]), creating a flow of ~1 ml/min into the lung inside the crystal ribcage. We imaged the exclusion of the dye inside the tumor bulk and up to ~100 μm away from it in the peritumoral

region indicating loss of circulatory functions in blood vessels remodeled by metastatic nodules (**Fig. 2i**). The fluorescence intensity was lower, and it took longer for the dye to reach inside the tumor bulk compared to the peritumor and unaffected capillaries far from the nodule (**Fig. 2j**). We also observed similar disruption of capillary function in the presence of dispersed single cancer cells before the tumors were established (**Extended Data Fig. 8, Supplemental Video 7**). We investigated the rate of passive diffusion in established nodular lung tumors, as convective flow was insufficient. Smaller molecular weight fluorescent CBhydrazide tracer (550 Da), was controllably perfused until background fluorescence reached steady state (**Fig. 2k**). By fitting a mathematical model based on the diffusion equation to the rate of increase in fluorescence intensity inside the tumor (see Methods), we estimated the diffusion coefficient of the tracer in nodular tumors, a key parameter determining the rate of the drug and nutrient delivery to the tumor core, to be 3.25 $\mu m^2/s$, consistent with what was reported in melanoma tumors[30].

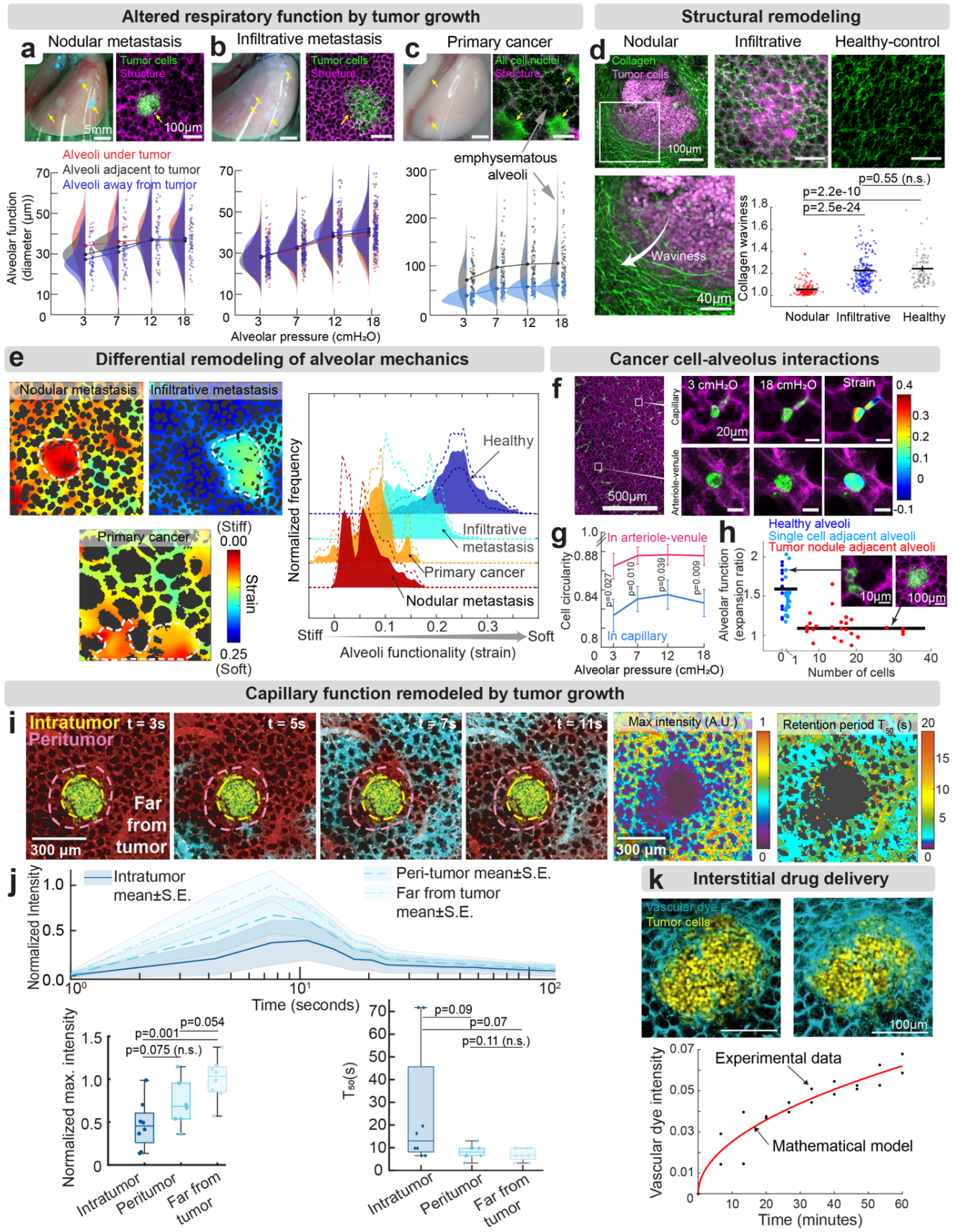
Altered respiratory function by tumor growth
a Nodular metastasis
b Infiltrative metastasis
c Primary cancer
Tumor cells
Structure
All cell nuclei
5mm
100µm
Alveoli under tumor
Alveoli adjacent to tumor
Alveoli away from tumor
emphysematous alveoli
Alveolar function (diameter (µm))
Alveolar pressure (cmH₂O)
Structural remodeling
d Nodular
Infiltrative
Healthy-control
Collagen
Tumor cells
Waviness
40µm
Collagen waviness
p=0.55 (n.s.)
p=2.2e-10
p=2.5e-24
Nodular
Infiltrative
Healthy
e Differential remodeling of alveolar mechanics
Nodular metastasis
Infiltrative metastasis
Primary cancer
(Stiff) 0.00
Strain
0.25 (Soft)
Normalized frequency
Healthy
Infiltrative metastasis
Primary cancer
Nodular metastasis
Stiff
Soft
Alveoli functionality (strain)
Cancer cell-alveolus interactions
f
Capillary
Arteriole-venule
500µm
3 cmH₂O
18 cmH₂O
Strain
20µm
g
In arteriole-venule
In capillary
Cell circularity
p=0.027
p=0.010
p=0.039
p=0.009
Alveolar pressure (cmH₂O)
h
Healthy alveoli
Single cell adjacent alveoli
Tumor nodule adjacent alveoli
Alveolar function (expansion ratio)
10µm
100µm
Number of cells
Capillary function remodeled by tumor growth
i
Intratumor
Peritumor
Far from tumor
t = 3s
t = 5s
t = 7s
t = 11s
300 µm
Max intensity (A.U.)
Retention period T₅₀ (s)
j
Intratumor mean±S.E.
Peri-tumor mean±S.E.
Far from tumor mean±S.E.
Normalized Intensity
Time (seconds)
Normalized max. intensity
p=0.001
p=0.054
p=0.075 (n.s.)
Intratumor
Peritumor
Far from tumor
T₅₀(s)
p=0.09
p=0.07
p=0.11 (n.s.)
k Interstitial drug delivery
vascular dye
Tumor cells
100µm
Vascular dye intensity
Experimental data
Mathematical model
Time (minutes)

247

FIGURE 2 | Multi-scale structure-function changes in lung cancer models. Tumors (yellow arrow) at whole-organ and alveolar scale, distribution of alveolar diameters measured intratumorally, peritumorally, and far from tumor at each quasi-static pressure, line connects mean of distribution **(a)** representative nodular metastasis (green) and alveoli (magenta), for m=4 ROI over n=3 mice, **(b)** representative infiltrative metastasis (green) and nearly fully functional alveoli (magenta), for m=4 ROI over n=3 mice, and **(c)** representative primary lung cancer nodules with adjacent emphysematous alveoli, for m=3 ROI over n=3 mice. **(d)** Second harmonic generation imaging of collagen architecture in nodular (m=7 ROI over n=3 mice) and infiltrative (m=7 ROI over n=2 mice) metastatic cancers, and healthy (m=4 ROI over n=1 mouse), mean line of the scatter data from k=150, 188, 92 fibers respectively. **(e)** Representative alveolar strain as lung pressure increases from 7 to 12 cmH_2O in each disease and mean ± SEM strain distribution per model for same ROI and mouse count in **a, b, c. (f)** Representative strain map of arrested cancer cells during quasi-static inflation in capillaries vs arterioles/venules. **(g)**. Bulk comparison of circularity of cancer cells tracked at different pressures taken from n=30 cells in arterioles/venules and n=40 cells in capillaries, mean ± SEM of data is presented, and significance is tested between cells in each group at each pressure. (**h**) Alveolar function decreases with increasing cells in cancer nodule. Individual data points represent nodules and lines are mean alveolar expansion ratio for nodules =< 1 cell and >2 cells from m=60 nodules over n=16 mice. **(i)** Real-time imaging of the disrupted capillary function through pressure-controlled perfusion of fluorescent Cascade Blue-dextran (10kDa), and **(j)** distribution and retention of the same for m=4 ROI over n=5 healthy mice and m=8 ROI over n=4 tumor bearing mice. **(k)** Passive diffusion of a small molecule tracer into the tumor bulk and the mathematically estimated diffusion coefficient (see Methods) of the tracer in the tumor. Boxplots present median with 25th and 75th percentiles, whiskers are the maximum and minimum data points not considered outliers. Comparison between groups performed with two-tailed Student's t-test for significance<0.05.

Respiratory and circulatory functions disrupted in pneumonia

Pneumonia has been a leading global burden of healthcare[31], even prior to the global COVID-19 crisis. Therefore, as another application of crystal ribcage, we decided to probe the impact of bacterial pneumonia infection and acute injury on lung respiratory and circulatory functions from the whole lobe down to single alveolus and single capillary scales. Imaging the whole lung showed that the hepatized left apex, was densely packed with MRP8+ neutrophils both at the whole lobe and alveolar scales (**Fig. 3a,b**). We examined the functionality of alveoli for quasi-static applied alveolar pressures (3-18 cmH_2O) similar to previous whole-lung pressure-volume curves characterized in mice[14,32,33]. The pressure-volume curves showed substantial heterogeneities (**Fig. 3**). Further analysis revealed that pneumonia-infected alveoli largely remained constant and were similar in size to healthy alveoli imaged at an alveolar pressure of 7 cmH_2O (**Fig. 3c**). Thus, infected alveoli are unable to respond (expand and contract) to pressure applied at the trachea due to both neutrophil recruitment and liquid influx into the airspace (pulmonary edema). We independently visualized neutrophil recruitment and pulmonary edema in infected alveoli simultaneously at the whole-lobe and single alveolus level (**Supplemental Fig. 8**) and found regions with high neutrophil recruitment closely match pulmonary edema (**Extended Data Fig. 9**). In comparison to disease-free alveoli, the inflammatory response to infection causes a decrease in strain at the lobar (**Supplementary Fig. 9a**) and alveolar scales (**Fig. 3d,e**) due partially to filling of the alveoli with incompressible liquid that increases local surface tension.

We next asked whether the recruitment of immune cells and edema in pneumonia affects capillary function and perfused a bolus of small molecule CBhydrazide (550 Da) fluorescent tracer to simulate a systemic drug delivered to treat infections. In real-time we mapped the heterogenous distribution (**Fig. 3f, Supplemental Video 8**) and intravascular delivery (**Fig. 3g,h**) of the perfusate near the infected regions, representing the retention and clearance of the drug. There was no difference in tracer arrival but delayed clearance from the infected region (**Fig. 3f,g**), as the duration of high fluorescence in pneumonia infected tissue was greater than adjacent healthy tissue

298 (**Fig. 3h**). This indicates that local vascular function is likely compromised in the injured alveoli,
299 causing the fluorescent tracer to leak into the interstitial space from the vascular space such that it
300 cannot be easily cleared by continuous perfusion. Additionally, vascular dynamics were slower in
301 the injured region in comparison to healthy tissue, suggesting that the dye was likely transported
302 by diffusion rather than convection in the injured tissue (**Fig 3f-i**). While it is unlikely that the
303 infected tissue is totally isolated from the rest of the pulmonary circulation, given that both healthy
304 and injured tissues experienced a comparable maximum fluorescence intensity upon the initial
305 arrival of the fluorescent tracer in the vasculature (**Fig. 3i**), the leakiness of vessels in pneumonia
306 potentially allowed the dye to be delivered faster than in metastatic tumors (**Supplementary Fig.**
307 **9b**).
308

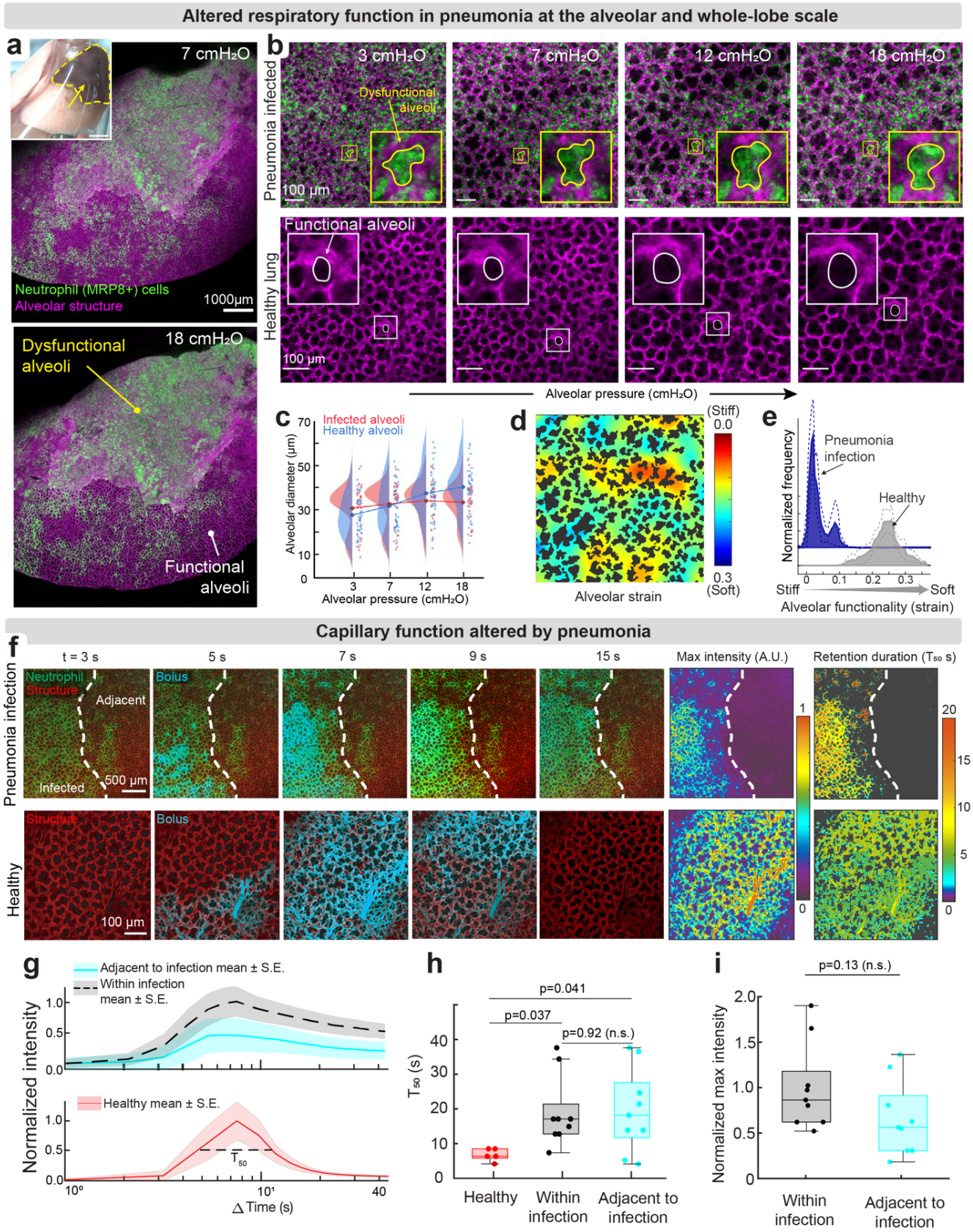
Altered respiratory function in pneumonia at the alveolar and whole-lobe scale
a
7 cmH₂O
Neutrophil (MRP8+) cells
Alveolar structure
1000µm
Dysfunctional alveoli
18 cmH₂O
Functional alveoli
b
Pneumonia infected
3 cmH₂O
7 cmH₂O
12 cmH₂O
18 cmH₂O
Dysfunctional alveoli
100 µm
Healthy lung
Functional alveoli
100 µm
Alveolar pressure (cmH₂O)
c
Infected alveoli
Healthy alveoli
Alveolar diameter (µm)
Alveolar pressure (cmH₂O)
d
(Stiff) 0.0
0.3 (Soft)
Alveolar strain
e
Pneumonia infection
Healthy
Normalized frequency
Stiff
Soft
Alveolar functionality (strain)
Capillary function altered by pneumonia
f
t = 3 s
5 s
7 s
9 s
15 s
Max intensity (A.U.)
Retention duration (T₅₀ s)
Pneumonia infection
Neutrophil
Structure
Adjacent
Bolus
Infected
500 µm
Healthy
Structure
Bolus
100 µm
g
Adjacent to infection mean ± S.E.
Within infection mean ± S.E.
Healthy mean ± S.E.
Normalized intensity
T50
Δ Time (s)
h
p=0.041
p=0.037
p=0.92 (n.s.)
T50 (s)
Healthy
Within infection
Adjacent to infection
i
p=0.13 (n.s.)
Normalized max intensity
Within infection
Adjacent to infection

309

FIGURE 3 | Impairment of alveolar respiratory and circulatory functions in pneumonia. (**a**) Entire left lobe imaged via confocal microscopy at 7 and 18 cmH_2O quasi-static alveolar pressures. (**b**). Representative images of alveolar deformation in a pneumonia-infected versus healthy lung in response to alveolar pressure changes. Single alveolus contoured shows dysfunctional alveoli (marked by neutrophil infiltration) are unresponsive to applied increases in air pressure compared to functional alveoli. (**c**) Distributed alveolar diameter data at each quasi-static pressure connected by the mean line for each infected and healthy groups for m=6 ROI over n=4 mice. (**d**) Representative strain map at alveolar scale strain showing reduced strain in neutrophil recruited areas. (**e**) Mean ± SEM of strain distribution in pneumonia infected and healthy regions, same mouse counts as **c**. (**f**) Capillary function in pneumonia infected and healthy lung perfused with CBhydrazide (550 Da) in RPMI medium at 15 cmH_2O pressure-controlled flow and an alveolar pressure of 7 cmH_2O. (**g**) Time course of fluorescence intensity in infected, infection-adjacent, and healthy capillaries. (**h**) Time duration when fluorescence intensity in the capillary bed was greater than 50% of the maximum intensity, indicating the tendency for dye to be retained in the capillary bed for m=4 ROI over n=5 healthy mice and m=9 ROI over n=4 pneumonia-infected mice. (**i**) Maximum fluorescence intensity in healthy and infection-adjacent capillaries after delivery of the bolus, for same mouse count as **h**. Boxplots present median with 25th and 75th percentiles, whiskers are the maximum and minimum data points not considered outliers. Comparison between groups performed with two-tailed Student's t-test for significance < 0.05.

Neutrophils are reversibly mechano-responsive

While we observed that recruitment of immune cells alters alveolar and capillary functions, we endeavored to see if the relationship was mutual, i.e., whether immune cell activity is also sensitive to changes in alveolar or capillary pressure. Neutrophil recruitment from pulmonary capillaries has differing rules, mechanisms, and constraints than from the systemic post-capillary venules[34-37]. Particularly, neutrophil emigration in the pneumonic lung is primarily from pulmonary capillaries rather than post capillary venules, as is characteristic of other tissues. Intravital microscopy has previously visualized neutrophil migration in the lung through implanted windows on the mouse ribcage[37,38]. However, these approaches cannot controllably alter alveolar and capillary pressures. We tracked single neutrophils in real-time while modulating alveolar and vascular pressures to probe the effects of breathing and circulation on pulmonary immunity.

We observed dramatic and reversible changes in neutrophil migration speed in response to an applied increase in vascular pressure in mouse models of lipopolysaccharide (LPS) injury and in bacterial pneumonia. It has been reported that the mean arterial pressure in the catheterized *in situ* resting mouse is 13-20 cmH_2O[39-41], and the left atrial pressure is approximately 5.4 cmH_2O[42]. We chose to apply a constant vascular pressure across the capillary bed of up to 15 cmH_2O[43,44] as an approximation of the pressure drop between the pulmonary artery and left atrium. In a lobar LPS model of acute injury in MRP8-mTmG mice[45,46] (**Fig. 4a**), we tracked neutrophils migrating within the injured alveoli in real-time and found that neutrophils migrated longer distances (**Fig. 4b**) and nearly twice as fast (**Fig. 4c**) at 15 cmH_2O compared to zero vascular pressure. This change in speed was also reversible, as neutrophil speed responded to repeated step-changes in vascular pressure (**Supplemental Video 9, Supplemental Fig. 10**). We maintained zero-flow conditions to decouple the effects of vascular flow and shear forces on immune cells[47]. We also measured the persistence (ratio of end-to-end displacement to distance travelled) and found that it did not increase with increasing vascular pressure in the lung implying the increase in cell motility is not flow-driven (**Fig. 4d**). Given no vascular flow and that neutrophil emigration was agnostic to pressure changes, it is unlikely that soluble chemokines (the majority of which are bound to proteoglycans) redistribute quickly enough to play a major role in our observed changes in migration speed. Additionally, the geometric and biophysical constraints posed by the lung capillaries largely prevent neutrophil rolling along endothelial cells, meaning that selectin binding

359 is an unlikely to be a strong contributor to the differences in migration speed we observe here[34-37].
360 Our results suggest that, within the complex environment of the lung capillary bed, neutrophils
361 either directly respond to changes in vascular pressure or they are indirectly influenced by other
362 factors that change with vascular pressure, such as vascular diameter, the surface density of
363 adhesion molecules and chemokines on the luminal surface of endothelial cells, or alteration in
364 cell junctions in response to stretch[48-51].
365
366 We independently confirmed the mechano-responsive behavior of neutrophils in bacterial
367 pneumonia (Sp3) infection. Imaging migration of neutrophils around infected alveoli (**Fig. 4e,f**)
368 revealed that cells located in the vascular and interstitial space migrated farther compared to
369 neutrophil inside the alveoli. Additionally, neutrophils in the vasculature and interstitium moved
370 almost twice as fast when vascular pressure was increased from 0 to 15 cmH_2O, while intra-
371 alveolar neutrophils remained slow regardless of vascular pressure changes (**Fig. 4g**). The
372 persistence of neutrophils in the pneumonia model was also independent of changes in vascular
373 pressure (**Fig. 4h**). We concurrently found that neutrophil speed did not respond to alveolar
374 pressure (**Fig. 4i**). Lastly, we observed that neutrophils dramatically changed shape while
375 migrating in lung capillaries and became more elliptical when moving faster (**Fig. 4j,**
376 **Supplemental Video 10**). We utilized the combined benefits of high controllability and intact
377 cellular diversity of the complex vascular architecture in the crystal ribcage to probe the mechano-
378 immunity of neutrophils, which potentially extends to other immune cell types[52].
379

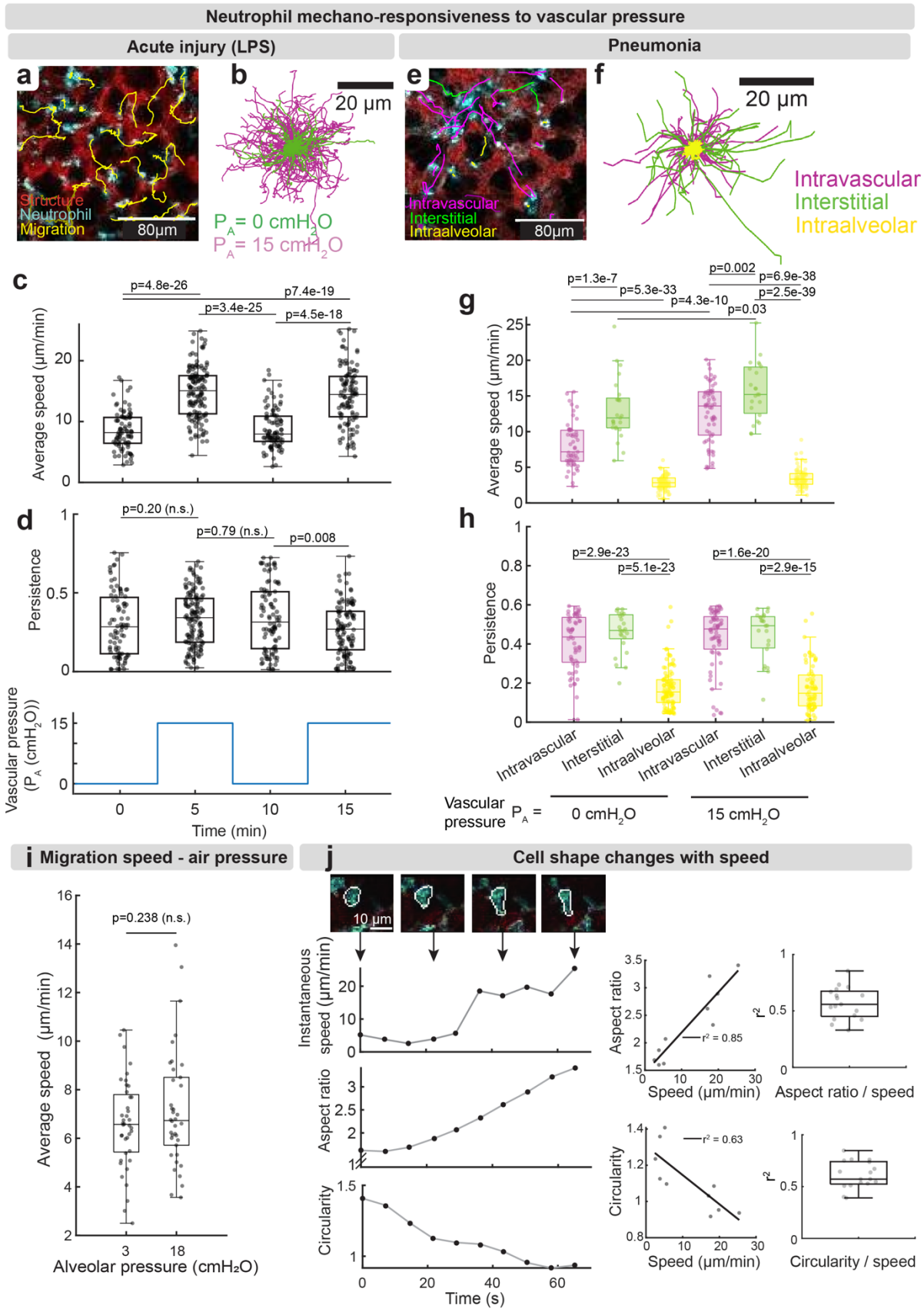
Neutrophil mechano-responsiveness to vascular pressure
Acute injury (LPS)
Pneumonia
a
Structure
Neutrophil
Migration
80µm
b
20 µm
P_A = 0 cmH_2O
P_A = 15 cmH_2O
e
Intravascular
Interstitial
Intraalveolar
80µm
f
20 µm
Intravascular
Interstitial
Intraalveolar
c
Average speed (µm/min)
p=4.8e-26
p7.4e-19
p=3.4e-25
p=4.5e-18
d
Persistence
p=0.20 (n.s.)
p=0.79 (n.s.)
p=0.008
Vascular pressure (P_A (cmH_2O))
Time (min)
g
Average speed (µm/min)
p=1.3e-7
p=5.3e-33
p=4.3e-10
p=0.002
p=6.9e-38
p=2.5e-39
p=0.03
h
Persistence
p=2.9e-23
p=5.1e-23
p=1.6e-20
p=2.9e-15
Intravascular
Interstitial
Intraalveolar
Intravascular
Interstitial
Intraalveolar
Vascular pressure P_A =
0 cmH_2O
15 cmH_2O
i Migration speed - air pressure
Average speed (µm/min)
p=0.238 (n.s.)
Alveolar pressure (cmH₂O)
j Cell shape changes with speed
10 µm
Instantaneous speed (µm/min)
Aspect ratio
Circularity
Time (s)
Aspect ratio
r² = 0.85
Speed (µm/min)
r²
Aspect ratio / speed
Circularity
r² = 0.63
Speed (µm/min)
r²
Circularity / speed

380

FIGURE 4 | Neutrophil migration is reversibly mechano-responsive to vascular pressure. (**a**) Representative image of neutrophil migration with cell trajectories (yellow) in the LPS model of acute lung injury. (**b**) Neutrophil migration map of paths travelled by single neutrophils over a 5-minute imaging interval. (**c**) Neutrophil average speed increases with vascular pressure and is reversible in LPS-damaged lungs (n=3 mice), for a constant alveolar pressure of 7 cmH_2O. (**d**) Persistence directionality of neutrophil migration in LPS-damaged lungs (n=3 mice). (**e**) Representative traced neutrophil migration in intra-alveolar (yellow), interstitial (green), and intravascular (magenta) spaces in Sp3 pneumonia lungs at a pulmonary artery pressure (PA) of 15 cmH_2O and a constant alveolar pressure of 7 cmH_2O. (**f**) Neutrophil migration map for 15 cmH_2O hydrostatic perfusion pressures and a constant alveolar pressure of 7 cmH_2O in pneumonia lungs for 5 minutes. (**g**) Neutrophil average speed and (**h**) persistence in intra-alveolar, interstitial, and intravascular spaces under 0 or 15 cmH_2O hydrostatic perfusion pressures in pneumonia lungs (n=3 mice), for a constant alveolar pressure of 7 cmH_2O. (**i**) Neutrophil average speed in pneumonia lungs under quasi-static alveolar pressures of 3 (m=38 neutrophil across n=2 mice) versus 18 cmH_2O (m=40 neutrophil across n=2 mice). (**j**) Representative changes in single neutrophil speed, aspect ratio, circularity of the same neutrophil with its respective aspect ratio vs. speed and circularity vs. speed linear regressions, and the regression coefficient of determination of aspect ratio vs. speed and circularity vs. speed of a population of neutrophils (m=27 cells over n=3 mice). Boxplots present median with 25th and 75th percentiles, whiskers are the maximum and minimum data points not considered outliers. Comparison between groups performed with two-tailed Student's t-test for significance < 0.05.

Respiration-circulation coupling is disrupted in lung injury

Lung respiration and circulation dynamics are strongly coupled. At the whole organ scale, this regulates the diameter of large blood vessels and in turn determines pulmonary vascular resistance[53]. To our knowledge respiration-circulation coupling has not been characterized at the alveolar-capillary scale. Hence, we quantified the effect of respiration-circulation coupling on capillary and arteriole/venule distension in healthy lungs by quasi-statically varying physiologically relevant alveolar and vascular pressure (**Fig. 5a**, **Supplemental Fig. 11**). We found the vascular diameter (inclusive of wall thickness and lumen width) in arterioles-venules to first increase and then decrease, creating a "bell shaped" curve across the applied vascular pressure range when alveolar pressure increased over the inspiratory range from 3 to 18 cmH_2O. This pressure response implies arteriole/venule diameter is maximized, resulting in a minimum vascular resistance, for an optimal range of alveolar pressures (7-12 cmH_2O) (**Fig. 5b**). Capillary diameter increased dramatically with increasing vascular pressure (**Fig. 5c**), but it started monotonically decreasing for alveolar pressures higher than 7 cmH_2O, for intermediate vascular pressures only (**Fig. 5c**). This indicated that alveolar pressures near 7 cmH_2O minimize vascular resistance in capillaries.

We contrasted the above findings with an acutely injured lung (LPS-treated) in which the parenchyma was substantially remodeled by an inflamed capillary bed and reduced alveolar size across the full breathing cycle (**Fig. 5d**). Respiration-circulation coupling is lost in injured capillaries, as increasing vascular pressure did little to increase vascular diameter. Increasing air pressure also did not reduce vascular diameter, compared to healthy capillaries (**Fig. 5e**). This disrupted the ability of the lung to respond to alveolar and blood pressure changes likely reduce local flow with loss of oxygen transport. The altered respiration-circulation coupling described above may also provide insight into neutrophils' mechano-responsiveness to pressure. We observed faster migration with increasing vascular pressure in neutrophil populations recruited to a bacterial pneumonia infected lung (**Fig. 5f**), which was accompanied by an increase in capillary diameter (**Fig. 5g**). However, increasing alveolar pressure in pneumonia-injured lungs did not alter neutrophil speeds (**Fig. 5f**), nor did it change capillary diameters (**Fig. 5g**). This correlation may suggest that tensional stresses on the luminal surface of the vasculature, due to increasing vascular

430 diameter, alters neutrophil migration speed by, potentially, facilitating binding of neutrophils to
431 the endothelial wall[54].
432
433 Lastly, we acutely perturbed the lung by injecting solid phase agarose (see Methods) in the
434 parenchyma to disrupt the respiration-circulation coupling. We found that alveoli near the agarose
435 were stiffened and largely unresponsive to quasi-static changes in alveolar pressure and excluded
436 perfused fluorescent dye, in contrast to alveoli farther away from the blockage (**Fig. 5h,**
437 **Supplemental Fig. 12, Supplemental Video 11**). This type of framework, where lung
438 functionality can be locally arrested, could be a useful model of Hypoxic Pulmonary
439 Vasoconstriction (HPV), where vessels contract in order to divert blood flow away from hypoxic
440 alveoli[55,56].
441

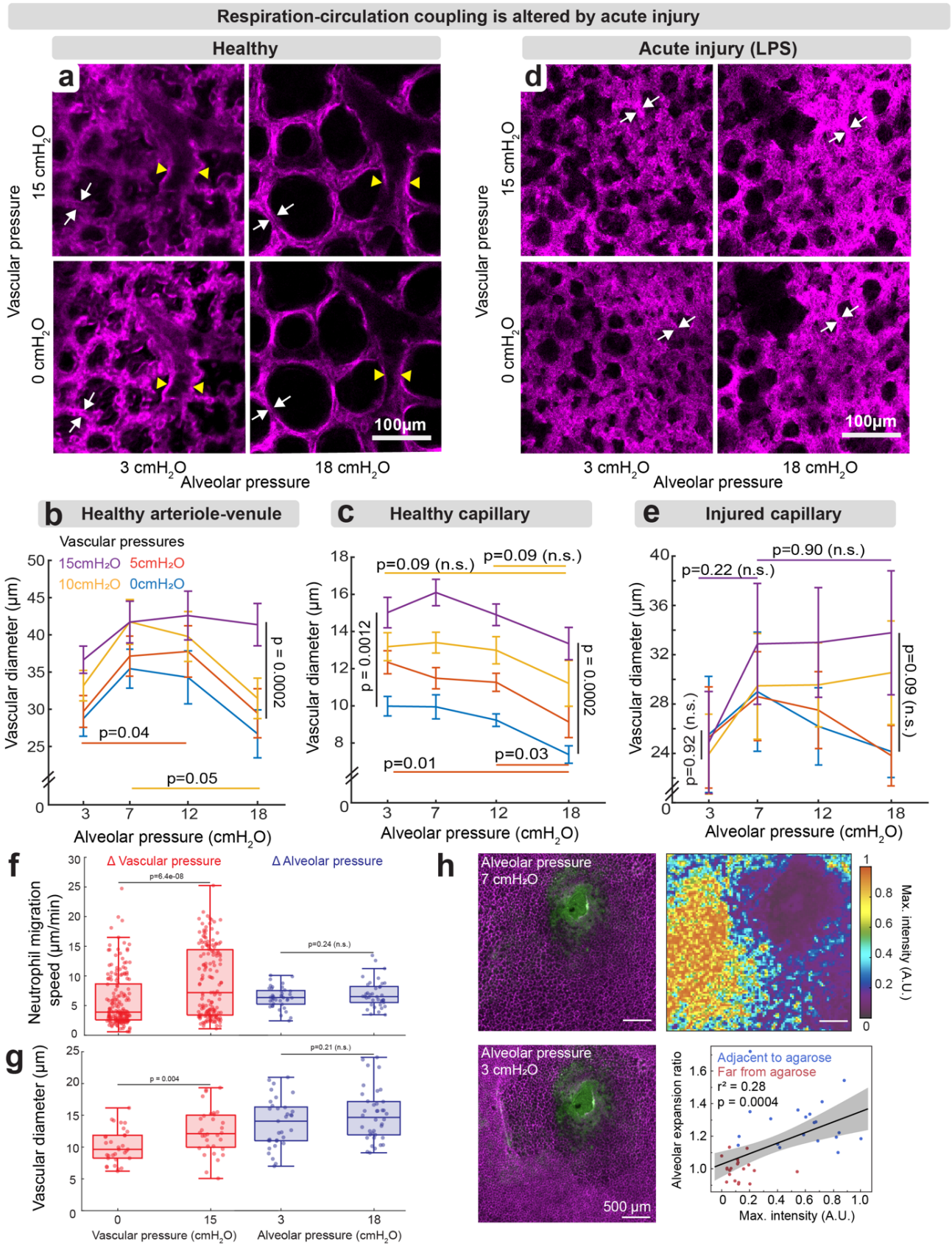
Respiration-circulation coupling is altered by acute injury
Healthy
Acute injury (LPS)
a
d
Vascular pressure
15 cmH2O
0 cmH2O
100µm
3 cmH2O
18 cmH2O
Alveolar pressure
b Healthy arteriole-venule
c Healthy capillary
e Injured capillary
Vascular pressures
15cmH2O 5cmH2O
10cmH2O 0cmH2O
Vascular diameter (µm)
Alveolar pressure (cmH2O)
p = 0.0002
p=0.04
p=0.05
p=0.09 (n.s.)
p = 0.0012
p=0.01
p=0.03
p=0.90 (n.s.)
p=0.22 (n.s.)
p=0.92 (n.s.)
p=0.09 (n.s.)
f
Δ Vascular pressure
Δ Alveolar pressure
Neutrophil migration speed (µm/min)
p=6.4e-08
p=0.24 (n.s.)
g
Vascular diameter (µm)
p = 0.004
p=0.21 (n.s.)
Vascular pressure (cmH2O)
Alveolar pressure (cmH2O)
h
Alveolar pressure 7 cmH2O
Alveolar pressure 3 cmH2O
500 µm
Max. intensity (A.U.)
Alveolar expansion ratio
Adjacent to agarose
Far from agarose
r² = 0.28
p = 0.0004

442

FIGURE 5 | Respiration-circulation coupling in healthy lungs and its disruption by acute injury. (**a**) Representative image of structural changes in the lung associated with variable quasi-static alveolar and vascular pressures, with measurements of diameter changes in single lung capillaries (white arrows) and large arterioles (yellow arrows), which can be tracked in the crystal ribcage across normal respiration-circulation parameters. Respiration-circulation coupling trends can be observed by measuring the vascular diameter in response to changing pressures in (**b**) large, heathy arterioles and venules (m=15 ROI over n=3 mice) and (**c**) healthy capillaries (m=19 ROI over n=4 mice). (**d**) Representative images of the injured lung after challenge with LPS, showing that single capillaries (white arrows) affected by acute injury (LPS) become inflamed and distend differently for the same pressure range. (**e**) Capillaries acutely injured after LPS challenge become non-responsive to changes in alveolar and vascular pressure (m=16 ROI over n=4 mice). All traces are presented as mean ± SEM and the p-value determined by testing groups using two-tailed Student's t-test for significance < 0.05. (**f**) Neutrophils migrate at faster speeds as vascular pressure measured at the pulmonary artery (PA) increases (m>130 neutrophils over n=2 mice) compared with little effect of increasing air pressure in the alveoli (m=40 neutrophils over n=2 mice). (**g**) Similarly vascular diameter changes are significantly different with increasing vascular pressure (n=2 mice), while changing alveolar pressure has little effect on it (n=2 mice). (**h**) Injecting Evans blue labeled agarose (green) produces a local blockage in the lung that disrupts alveolar-capillary function, as alveoli near the blockage do not deform across quasi-static air pressures and exclude perfused fluorescent tracer, while alveoli and capillaries farther away from the blockage remain functional (m=40 alveoli over n=1 mouse).

Discussion

We have developed the crystal ribcage technology and demonstrated its capabilities for probing lung function and dysfunction across nearly the entire surface at the whole-organ, alveolar and cellular scales in real-time. The crystal ribcage enables multi-scale imaging of respiratory and circulatory functions while preserving the native 3-D architecture and cellular diversity of the lung in a wide array of pulmonary diseases (**Fig. 1**). In cancer, we found (i) differential remodeling of alveolar function in nodular vs infiltrative (co-optive) growth pattern, (ii) earliest stages of tumorigenesis that compromises alveolar respiratory function, and (iii) compromised capillary function around a nodular tumor (**Fig. 2**). We also demonstrated altered respiratory and circulatory functions in pneumonia, which affects delivery of oxygen, nutrient, and therapeutics, and impairs trafficking, recruitment, and clearance of immune cells (**Fig. 3**). By modulating vascular pressure in the lung, we found that neutrophils are strongly and reversibly mechano-responsive to vascular pressure in a mouse model of pneumonia and acute lung injury (**Fig. 4**). While more work needs to be done to understand the underlying mechanisms, the controllability of lung physiology in the crystal ribcage (e.g., vascular pressure in this application) provides enormous opportunity for understanding cause-and-effect in pulmonary pathogenesis. Lastly, we demonstrated that respiration-circulation coupling at the capillary level and found that this coupling is eliminated in acute injury (**Fig. 5**).

While the crystal ribcage supports probing of several lung diseases with parenchymal presentation, deeper imaging could expand the capabilities of our platform. Currently, any optical imaging modality is depth-limited in the lung due to light diffraction at the air-liquid interfaces of the alveoli[7,8], a limitation unrelated to the crystal ribcage itself. When the alveoli are filled with liquid (e.g. edema) or cancer cells, light scattering is reduced which enables imaging up to 500 μm deep as opposed to 100 μm in air-filled alveoli (**Extended Data Fig. 6**). While the crystal ribcage allows dynamic imaging at physiological respiratory and circulatory rates (**Supplemental video 2,3**), we chose to probe the lung mechanics under quasi-static conditions to be able to report the accurate pressure values in the alveoli and capillaries. Ultrafast volumetric imaging techniques coupled

with the crystal ribcage can resolve respiration and circulation dynamics at the "speed of life", fast cell-cell communications such as calcium signaling, and quantify viscoelastic properties and energy dissipation at the alveolar level, all in a functioning lung. Additionally, recent optical imaging approaches[57] to measure partial oxygen pressure could be leveraged to study gas transport in single alveoli[58] in the crystal ribcage.

The crystal ribcage can also be used to image heart function in real-time. We imaged the pulsing of the heart atrium on the ventral surface of the crystal ribcage in response to elevated vascular pressure (**Extended Data Fig. 10, Supplemental Video 12**). Such experiments will allow further probing of circulation-respiration coupling in diseases such as pulmonary hypertension or arrhythmia in the future. Disease models, here, were developed *in vivo* on the order of days to weeks, and we probed the underlying physiology and pathology for 4-6 hours *ex vivo* inside the crystal ribcage, sufficient for studying dynamic events such respiratory function, immune cell migration, and circulation dynamics. However, recent studies have maintained human lungs up to 24 hours *ex vivo* [59] , pig lungs up to 3 days[60] and rats up to 7 days[61]. Utilizing these advances[62], we will adapt the crystal ribcage to maintain lung viability for multi-day studies of disease dynamics. We are also taking advantage of the scalability of our fabrication process to develop the crystal ribcage for large animals such as pig and transplant-rejected human lungs[63] to probe diseases and therapeutics in a more clinically relevant setting.

Acknowledgements: We thank the Neurophotonics Center at Boston University for their generous support and access to their facility. Adam Coats from the Hoffman lab at the University of Iowa provided the μCT image data sets used to fabricate the crystal ribcage. The research reported in this publication was supported by the Boston University Micro and Nano Imaging Facility and the Office of the Director, National Institutes of Health of the National Institutes of Health under award Number S10OD024993. The content is solely the responsibility of the authors and does not necessarily represent the official views of the National Institute of Health. Any opinion, findings, and conclusions or recommendations expressed in this material are those of the authors and do not necessarily reflect the views of the National Science Foundation.

Author contributions: R.B., G.N.G. and H.T.N. conceived the project and wrote the manuscript; R.B. developed and validated the crystal ribcages and external devices suite, established transgenic mouse colonies, analyzed alveolar function, strain maps and collagen waviness; G.N.G. conducted the lung extraction and imaging, generated experimental mice, cultured cancer cells, and analyzed circulatory function data; L.S. analyzed perfusion, vascular transport, and neutrophil mechano-responsiveness data; D.S. analyzed alveolar and capillary function data, and maintained animal colony; R.L. developed registration and strain analysis algorithm; J.M. developed custom hardware for crystal ribcage and analyzed alveolar function data; C.E. developed the deformable crystal ribcage; B.E.H. generated the lobar pneumonia mouse model; J.L. and A.A.R. generated the fibrosis model; A.A.R. performed the histology and staining for fibrotic lungs; J.C.B. generated primary cancer mice, K.R. analyzed alveolar function data and cultured cancer cells; S. Zheng cultured cancer cells; S. Zhang fabricated fluorescent polyacrylamide beads; J.J. assisted in surgical techniques for *in situ* lung imaging; R.P. generated LPS induction model; K.T. provided transgenic MPR8-Cre^{+} mouse; S.M., G.L., J.P.M. and B.S. contributed to discussion on crucial aspects of the project; H.T.N. supervised the project and provided guidance on experimental design, data collection, data interpretation, and writing of the manuscript.

Funding: H.T.N. discloses support for the research described in this study from the National Institutes of Health R21EB031332 and DP2HL168562, Beckman Young Investigator Award, Johnson & Johnson Lung Cancer Initiative, Boston University Center for Multiscale and Translational Mechanobiology, and Dean's Catalyst Award, and the American Cancer Society Institutional Fund at Boston University. L.S. acknowledges support from the National Heart, Lung, and Blood Institute Grant 1F30HL168952-01. This material is also based upon work supported by the National Science Foundation, and G.N.G acknowledges support from the NSF Graduate Research Fellowship, Grant No. 2234657.The funders had no role in study design, data collection and analysis, decision to publish or preparation of the manuscript.

Competing interests: H.T.N has received research funding from Johnson & Johnson Lung Cancer Initiative at Boston University. The funding has supported the development of the lung cancer models described in the manuscript. All other authors report no competing interests.

References

1 Entenberg, D. *et al.* A permanent window for the murine lung enables high-resolution imaging of cancer metastasis. *Nat Methods* **15**, 73-80 (2018). https://doi.org:10.1038/nmeth.4511

2 Headley, M. B. *et al.* Visualization of immediate immune responses to pioneer metastatic cells in the lung. *Nature* **531**, 513-517 (2016). https://doi.org:10.1038/nature16985

3 Looney, M. R. *et al.* Stabilized imaging of immune surveillance in the mouse lung. *Nat Methods* **8**, 91-96 (2011). https://doi.org:10.1038/nmeth.1543

4 Ueki, H., Wang, I. H., Zhao, D., Gunzer, M. & Kawaoka, Y. Multicolor two-photon imaging of in vivo cellular pathophysiology upon influenza virus infection using the two-photon IMPRESS. *Nat Protoc* **15**, 1041-1065 (2020). https://doi.org:10.1038/s41596-019-0275-y

5 Westphalen, K. *et al.* Sessile alveolar macrophages communicate with alveolar epithelium to modulate immunity. *Nature* **506**, 503-506 (2014). https://doi.org:10.1038/nature12902

6 Borriello, L. *et al.* Primary tumor associated macrophages activate programs of invasion and dormancy in disseminating tumor cells. *Nat Commun* **13**, 626 (2022). https://doi.org:10.1038/s41467-022-28076-3

7 Lefrancais, E. *et al.* The lung is a site of platelet biogenesis and a reservoir for haematopoietic progenitors. *Nature* **544**, 105-109 (2017). https://doi.org:10.1038/nature21706

8 Hassell, B. A. *et al.* Human Organ Chip Models Recapitulate Orthotopic Lung Cancer Growth, Therapeutic Responses, and Tumor Dormancy In Vitro. *Cell Rep* **21**, 508-516 (2017). https://doi.org:10.1016/j.celrep.2017.09.043

9 Haudebourg, A. F. *et al.* Respiratory Mechanics of COVID-19- versus Non-COVID-19-associated Acute Respiratory Distress Syndrome. *Am J Respir Crit Care Med* **202**, 287-290 (2020). https://doi.org:10.1164/rccm.202004-1226LE

10 Lederer, D. J. & Martinez, F. J. Idiopathic Pulmonary Fibrosis. *N Engl J Med* **378**, 1811-1823 (2018). https://doi.org:10.1056/NEJMra1705751

11 Suki, B. *et al.* Emphysema and mechanical stress-induced lung remodeling. *Physiology (Bethesda)* **28**, 404-413 (2013). https://doi.org:10.1152/physiol.00041.2013

12 Huh, D. *et al.* Reconstituting organ-level lung functions on a chip. *Science* **328**, 1662-1668 (2010). https://doi.org:10.1126/science.1188302

13 Hall, J. E. *Guyton and hall textbook of medical physiology*. 14. edn, (Elsevier, 2020).

14 Limjunyawong, N., Fallica, J., Horton, M. R. & Mitzner, W. Measurement of the pressure-volume curve in mouse lungs. *J Vis Exp*, 52376 (2015). https://doi.org:10.3791/52376

15 Collaborators, G. B. D. R. T. C. Global, regional, and national burden of respiratory tract cancers and associated risk factors from 1990 to 2019: a systematic analysis for the Global Burden of Disease Study 2019. *Lancet Respir Med* **9**, 1030-1049 (2021). https://doi.org:10.1016/S2213-2600(21)00164-8

16 Stella, G. M., Kolling, S., Benvenuti, S. & Bortolotto, C. Lung-Seeking Metastases. *Cancers (Basel)* **11** (2019). https://doi.org:10.3390/cancers11071010

17 Seano, G. *et al.* Solid stress in brain tumours causes neuronal loss and neurological dysfunction and can be reversed by lithium. *Nat Biomed Eng* **3**, 230-245 (2019). https://doi.org:10.1038/s41551-018-0334-7

18 Donnem, T. *et al.* Non-angiogenic tumours and their influence on cancer biology. *Nat Rev Cancer* **18**, 323-336 (2018). https://doi.org:10.1038/nrc.2018.14

19 Griveau, A. *et al.* A Glial Signature and Wnt7 Signaling Regulate Glioma-Vascular Interactions and Tumor Microenvironment. *Cancer Cell* **33**, 874-889 e877 (2018). https://doi.org:10.1016/j.ccell.2018.03.020

20 Zhang, S. *et al.* The peritumor microenvironment: physics and immunity. *Trends Cancer* (2023). https://doi.org:10.1016/j.trecan.2023.04.004

21 Conklin, M. W. *et al.* Aligned collagen is a prognostic signature for survival in human breast carcinoma. *Am J Pathol* **178**, 1221-1232 (2011). https://doi.org:10.1016/j.ajpath.2010.11.076

22 Provenzano, P. P. *et al.* Collagen reorganization at the tumor-stromal interface facilitates local invasion. *BMC Med* **4**, 38 (2006). https://doi.org:10.1186/1741-7015-4-38

23 Baskaran, J. P. *et al.* Cell shape, and not 2D migration, predicts extracellular matrix-driven 3D cell invasion in breast cancer. *APL Bioeng* **4**, 026105 (2020). https://doi.org:10.1063/1.5143779

24 Zhang, S. *et al.* In vivo multiscale measurements of solid stresses in tumors reveal scale-dependent stress transmission. *Nature Biomedical Engineering* **In press** (2023). https://doi.org:10.21203/rs.3.rs-1697924/v1

25 Nia, H. T. *et al.* Quantifying solid stress and elastic energy from excised or in situ tumors. *Nat Protoc* **13**, 1091-1105 (2018). https://doi.org:10.1038/nprot.2018.020

26 Nia, H. T. *et al.* In vivo compression and imaging in mouse brain to measure the effects of solid stress. *Nat Protoc* **15**, 2321-2340 (2020). https://doi.org:10.1038/s41596-020-0328-2

27 Nia, H. T. *et al.* Solid stress and elastic energy as measures of tumour mechanopathology. *Nat Biomed Eng* **1** (2016). https://doi.org:10.1038/s41551-016-0004

28 Nia, H. T., Munn, L. L. & Jain, R. K. Physical traits of cancer. *Science* **370** (2020). https://doi.org:10.1126/science.aaz0868

29 Thibault, H. B. *et al.* Noninvasive assessment of murine pulmonary arterial pressure: validation and application to models of pulmonary hypertension. *Circ Cardiovasc Imaging* **3**, 157-163 (2010). https://doi.org:10.1161/CIRCIMAGING.109.887109

30 Alexandrakis, G. *et al.* Two-photon fluorescence correlation microscopy reveals the two-phase nature of transport in tumors. *Nat Med* **10**, 203-207 (2004). https://doi.org:10.1038/nm981

31 Murdoch, D. R. & Howie, S. R. C. The global burden of lower respiratory infections: making progress, but we need to do better. *Lancet Infect Dis* **18**, 1162-1163 (2018). https://doi.org:10.1016/S1473-3099(18)30407-9

32 Eckle, T., Fullbier, L., Grenz, A. & Eltzschig, H. K. Usefulness of pressure-controlled ventilation at high inspiratory pressures to induce acute lung injury in mice. *Am J Physiol Lung Cell Mol Physiol* **295**, L718-724 (2008). https://doi.org:10.1152/ajplung.90298.2008

33 Soutiere, S. E. & Mitzner, W. On defining total lung capacity in the mouse. *J Appl Physiol (1985)* **96**, 1658-1664 (2004). https://doi.org:10.1152/japplphysiol.01098.2003

34 Mizgerd, J. P. Molecular mechanisms of neutrophil recruitment elicited by bacteria in the lungs. *Semin Immunol* **14**, 123-132 (2002). https://doi.org:10.1006/smim.2001.0349

35 Mizgerd, J. P. Acute lower respiratory tract infection. *N Engl J Med* **358**, 716-727 (2008). https://doi.org:10.1056/NEJMra074111

36 Quinton, L. J. & Mizgerd, J. P. Dynamics of lung defense in pneumonia: resistance, resilience, and remodeling. *Annu Rev Physiol* **77**, 407-430 (2015). https://doi.org:10.1146/annurev-physiol-021014-071937

37 Quinton, L. J., Walkey, A. J. & Mizgerd, J. P. Integrative Physiology of Pneumonia. *Physiol Rev* **98**, 1417-1464 (2018). https://doi.org:10.1152/physrev.00032.2017

38 Lefrancais, E., Mallavia, B., Zhuo, H., Calfee, C. S. & Looney, M. R. Maladaptive role of neutrophil extracellular traps in pathogen-induced lung injury. *JCI Insight* **3** (2018). https://doi.org:10.1172/jci.insight.98178

39 Gomez-Arroyo, J. *et al.* A brief overview of mouse models of pulmonary arterial hypertension: problems and prospects. *Am J Physiol Lung Cell Mol Physiol* **302**, L977-991 (2012). https://doi.org:10.1152/ajplung.00362.2011

40 Vanderpool, R. R., Kim, A. R., Molthen, R. & Chesler, N. C. Effects of acute Rho kinase inhibition on chronic hypoxia-induced changes in proximal and distal pulmonary arterial structure and function. *J Appl Physiol (1985)* **110**, 188-198 (2011). https://doi.org:10.1152/japplphysiol.00533.2010

41 Xiong, M. *et al.* Mouse model of experimental pulmonary hypertension: Lung angiogram and right heart catheterization. *Pulm Circ* **11**, 20458940211041512 (2021). https://doi.org:10.1177/20458940211041512

42 Friedrich, E. E. *et al.* Endothelial cell Piezo1 mediates pressure-induced lung vascular hyperpermeability via disruption of adherens junctions. *Proc Natl Acad Sci U S A* **116**, 12980-12985 (2019). https://doi.org:10.1073/pnas.1902165116

43 Tuchscherer, H. A., Vanderpool, R. R. & Chesler, N. C. Pulmonary vascular remodeling in isolated mouse lungs: effects on pulsatile pressure-flow relationships. *J Biomech* **40**, 993-1001 (2007). https://doi.org:10.1016/j.jbiomech.2006.03.023

44 Vanderpool, R. R. & Chesler, N. C. Characterization of the isolated, ventilated, and instrumented mouse lung perfused with pulsatile flow. *J Vis Exp* (2011). https://doi.org:10.3791/2690

45 Domscheit, H., Hegeman, M. A., Carvalho, N. & Spieth, P. M. Molecular Dynamics of Lipopolysaccharide-Induced Lung Injury in Rodents. *Front Physiol* **11**, 36 (2020). https://doi.org:10.3389/fphys.2020.00036

46 Mitchell, M. J., Lin, K. S. & King, M. R. Fluid shear stress increases neutrophil activation via platelet-activating factor. *Biophys J* **106**, 2243-2253 (2014). https://doi.org:10.1016/j.bpj.2014.04.001

47 Huse, M. Mechanical forces in the immune system. *Nat Rev Immunol* **17**, 679-690 (2017). https://doi.org:10.1038/nri.2017.74

48 Kelly, G. T. *et al.* Pulmonary Endothelial Mechanical Sensing and Signaling, a Story of Focal Adhesions and Integrins in Ventilator Induced Lung Injury. *Front Physiol* **10**, 511 (2019). https://doi.org:10.3389/fphys.2019.00511

49 Lai, Y. & Huang, Y. Mechanisms of Mechanical Force Induced Pulmonary Vascular Endothelial Hyperpermeability. *Front Physiol* **12**, 714064 (2021). https://doi.org:10.3389/fphys.2021.714064

50 Shiraishi, K. *et al.* Biophysical forces mediated by respiration maintain lung alveolar epithelial cell fate. *Cell* **186**, 1478-1492 e1415 (2023). https://doi.org:10.1016/j.cell.2023.02.010

51 Zhong, M. *et al.* Alveolar Stretch Activation of Endothelial Piezo1 Protects Adherens Junctions and Lung Vascular Barrier. *Am J Respir Cell Mol Biol* **62**, 168-177 (2020). https://doi.org:10.1165/rcmb.2019-0024OC

52 Jones, D. *et al.* Solid stress impairs lymphocyte infiltration into lymph-node metastases. *Nat Biomed Eng* **5**, 1426-1436 (2021). https://doi.org:10.1038/s41551-021-00766-1

53 Whipp, B. J. & Ward, S. A. Cardiopulmonary coupling during exercise. *J Exp Biol* **100**, 175-193 (1982). https://doi.org:10.1242/jeb.100.1.175

54 Phillipson, M. & Kubes, P. The neutrophil in vascular inflammation. *Nat Med* **17**, 1381-1390 (2011). https://doi.org:10.1038/nm.2514

55 Hussain, A., Suleiman, M. S., George, S. J., Loubani, M. & Morice, A. Hypoxic Pulmonary Vasoconstriction in Humans: Tale or Myth. *Open Cardiovasc Med J* **11**, 1-13 (2017). https://doi.org:10.2174/1874192401711010001

56 Sylvester, J. T., Shimoda, L. A., Aaronson, P. I. & Ward, J. P. Hypoxic pulmonary vasoconstriction. *Physiol Rev* **92**, 367-520 (2012). https://doi.org:10.1152/physrev.00041.2010

57 Sakadzic, S. *et al.* Two-photon high-resolution measurement of partial pressure of oxygen in cerebral vasculature and tissue. *Nat Methods* **7**, 755-759 (2010). https://doi.org:10.1038/nmeth.1490

58 Butler, J. P. & Tsuda, A. Transport of gases between the environment and alveoli--theoretical foundations. *Compr Physiol* **1**, 1301-1316 (2011). https://doi.org:10.1002/cphy.c090016

59 Cardenes, N. *et al.* Human ex vivo lung perfusion: a novel model to study human lung diseases. *Sci Rep* **11**, 490 (2021). https://doi.org:10.1038/s41598-020-79434-4

60 Ali, A. *et al.* Successful 3-day lung preservation using a cyclic normothermic ex vivo lung perfusion strategy. *EBioMedicine* **83**, 104210 (2022). https://doi.org:10.1016/j.ebiom.2022.104210

61 Petersen, T. H., Calle, E. A., Colehour, M. B. & Niklason, L. E. Bioreactor for the long-term culture of lung tissue. *Cell Transplant* **20**, 1117-1126 (2011). https://doi.org:10.3727/096368910X544933

62 Loor, G. *et al.* Prolonged EVLP Using OCS Lung: Cellular and Acellular Perfusates. *Transplantation* **101**, 2303-2311 (2017). https://doi.org:10.1097/TP.0000000000001616

63 Hozain, A. E. *et al.* Xenogeneic cross-circulation for extracorporeal recovery of injured human lungs. *Nat Med* **26**, 1102-1113 (2020). https://doi.org:10.1038/s41591-020-0971-8

64 Muzumdar, M. D., Tasic, B., Miyamichi, K., Li, L. & Luo, L. A global double-fluorescent Cre reporter mouse. *Genesis* **45**, 593-605 (2007). https://doi.org:10.1002/dvg.20335

65 Passegue, E., Wagner, E. F. & Weissman, I. L. JunB deficiency leads to a myeloproliferative disorder arising from hematopoietic stem cells. *Cell* **119**, 431-443 (2004). https://doi.org:10.1016/j.cell.2004.10.010

66 Barker, K. A. *et al.* Lung-resident memory B cells protect against bacterial pneumonia. *J Clin Invest* **131** (2021). https://doi.org:10.1172/JCI141810

728 67 Kitzerow, O., Zucker, I. H., Lisco, S. J. & Wang, H. J. Timeline of Multi-Organ Plasma
729 Extravasation After Bleomycin-Induced Acute Lung Injury. *Front Physiol* **13**, 777072
730 (2022). https://doi.org:10.3389/fphys.2022.777072
731 68 Mammoto, A. *et al.* Control of lung vascular permeability and endotoxin-induced
732 pulmonary oedema by changes in extracellular matrix mechanics. *Nat Commun* **4**, 1759
733 (2013). https://doi.org:10.1038/ncomms2774
734 69 Smith, P., Jeffers, L. A. & Koval, M. Measurement of Lung Vessel and Epithelial
735 Permeability In Vivo with Evans Blue. *Methods Mol Biol* **2367**, 137-148 (2021).
736 https://doi.org:10.1007/7651_2020_345
737 70 Kassie, F., Matise, I., Negia, M., Upadhyaya, P. & Hecht, S. S. Dose-dependent
738 inhibition of tobacco smoke carcinogen-induced lung tumorigenesis in A/J mice by
739 indole-3-carbinol. *Cancer Prev Res (Phila)* **1**, 568-576 (2008).
740 https://doi.org:10.1158/1940-6207.CAPR-08-0064
741 71 Mizgerd, J. P., Scott, M. L., Spieker, M. R. & Doerschuk, C. M. Functions of IkappaB
742 proteins in inflammatory responses to Escherichia coli LPS in mouse lungs. *Am J Respir*
743 *Cell Mol Biol* **27**, 575-582 (2002). https://doi.org:10.1165/rcmb.2002-0015OC
744 72 Caporarello, N. *et al.* Dysfunctional ERG signaling drives pulmonary vascular aging and
745 persistent fibrosis. *Nat Commun* **13**, 4170 (2022). https://doi.org:10.1038/s41467-022-
746 31890-4
747 73 Suki, B., Bartolak-Suki, E. & Rocco, P. R. M. Elastase-Induced Lung Emphysema
748 Models in Mice. *Methods Mol Biol* **1639**, 67-75 (2017). https://doi.org:10.1007/978-1-
749 4939-7163-3_7
750 74 Banerji, R., Grifno, G. N. & Nia, H. T. Design and development of a novel Crystal
751 ribcage for probing real-time lung function at cellular resolution in health and disease.
752 *Protocol Exchange on Research Square* (2023).
753 https://doi.org:https://doi.org/10.21203/rs.3.pex-2253/v1
754 75 Kizhakke Puliyakote, A. S. *et al.* Morphometric differences between central vs. surface
755 acini in A/J mice using high-resolution micro-computed tomography. *J Appl Physiol*
756 *(1985)* **121**, 115-122 (2016). https://doi.org:10.1152/japplphysiol.00317.2016
757 76 Thiesse, J. *et al.* Lung structure phenotype variation in inbred mouse strains revealed
758 through in vivo micro-CT imaging. *J Appl Physiol (1985)* **109**, 1960-1968 (2010).
759 https://doi.org:10.1152/japplphysiol.01322.2009
760 77 Vasilescu, D. M. *et al.* Stereological assessment of mouse lung parenchyma via
761 nondestructive, multiscale micro-CT imaging validated by light microscopic histology. *J*
762 *Appl Physiol (1985)* **114**, 716-724 (2013).
763 https://doi.org:10.1152/japplphysiol.00855.2012
764 78 Schulte, H., Muhlfeld, C. & Brandenberger, C. Age-Related Structural and Functional
765 Changes in the Mouse Lung. *Front Physiol* **10**, 1466 (2019).
766 https://doi.org:10.3389/fphys.2019.01466
767 79 Gokaltun, A., Kang, Y. B. A., Yarmush, M. L., Usta, O. B. & Asatekin, A. Simple
768 Surface Modification of Poly(dimethylsiloxane) via Surface Segregating Smart Polymers
769 for Biomicrofluidics. *Sci Rep* **9**, 7377 (2019). https://doi.org:10.1038/s41598-019-43625-
770 5
771 80 Allen, M., Poggiali, D., Whitaker, K., Marshall, T. R. & Kievit, R. A. Raincloud plots: a
772 multi-platform tool for robust data visualization. *Wellcome Open Res* **4**, 63 (2019).
773 https://doi.org:10.12688/wellcomeopenres.15191.1

81 Heinrich, M. P., Jenkinson, M., Brady, M. & Schnabel, J. A. MRF-based deformable registration and ventilation estimation of lung CT. *IEEE Trans Med Imaging* **32**, 1239-1248 (2013). https://doi.org:10.1109/TMI.2013.2246577

82 Banerji, R., Shi, L., LeBourdais, R. & Nia, H. T. Development and demonstration of software tools to complement the real-time cellular resolution imaging capabilities of the crystal ribcage (1.0.0). . *Zenodo* (2023). https://doi.org:10.5281/zenodo.7939073

83 Hozain, A. E. *et al.* Multiday maintenance of extracorporeal lungs using cross-circulation with conscious swine. *J Thorac Cardiovasc Surg* **159**, 1640-1653 e1618 (2020). https://doi.org:10.1016/j.jtcvs.2019.09.121

84 Vrselja, Z. *et al.* Restoration of brain circulation and cellular functions hours post-mortem. *Nature* **568**, 336-343 (2019). https://doi.org:10.1038/s41586-019-1099-1

85 Eshmuminov, D. *et al.* An integrated perfusion machine preserves injured human livers for 1 week. *Nat Biotechnol* **38**, 189-198 (2020). https://doi.org:10.1038/s41587-019-0374-x

Methods

Mice

All experiments conformed to ethical principles and guidelines under protocols approved by the Boston University Institutional Animal Care and Use Committee. Mice were housed and bred under pathogen–free, ambient temperature, humidity, and light-dark conditions at the Boston University Animal Science Center, no housing or handling exceptions were made for this study. We used 6–12-week-old male and female mice for the experimental procedures. Female FVB mice aged 6-8 weeks (JAX #001800, Jackson Labs, ME) were purchased. A breeding pair of transgenic B6.129(Cg)-Gt(ROSA)26Sortm4(ACTB-tdTomato,-EGFP)Luo/J (JAX #007676, Jackson lab, ME)[64], hereafter referred to as mTmG, was purchased to start a colony and was the primary source of all animals for the experiments. Male neutrophil reporter mice B6.Cg-Tg(S100A8-cre,-EGFP)1Ilw/J (JAX #021614)[65] were purchased from JAX and crossed with in-house homozygous mTmG females to breed MRP8-mTmG mice that were used for neutrophil migration dynamics. We used a 6-week SPC-GFP mouse (Jax #028356) to visualize alveolar epithelial type II cells.

Metastatic cancer model

E0771-H2B-dendra2 mouse cancer cells or MCa-M3C-H2B-dendra2 (both gifts from Rakesh Jain) were used to model breast cancer metastasis to the lung in mTmG and FVB mice, respectively. Cells were cultured in DMEM (Corning) plus 10% fetal bovine serum (Gibco) plus 1% penicillin/streptomycin (Gibco). Cells were harvested at ~80% confluency, washed twice with phosphate buffered saline (PBS), counted, and resuspended in DMEM prior to tail vein injection into mice at a concentration of 2 million per 300uL complete medium. All cell lines tested negative for mycoplasma (Mycoalert Plus Mycoplasma Detection Kit, Lonza, Allendale, NJ), and authenticated before use by IDEXX laboratories (North Grafton, MA). Mice injected with E0771-H2B-dendra2 were sacrificed on days 5-7 post injection for microscopy of mature nodules. Mice injected with MCa-M3C-H2B-dendra2 were sacrificed on days 10-14 for microscopy of mature nodules. Largest tumor nodules studied were 2 mm in diameter and mice were excluded from the study if they presented with labored breathing, hunched posture, or ruffled fur due to tumor progression (as stipulated by BU IACUC). For single cell deformation studies, E0771-H2B-dendra2 cells were plasma membrane labeled with 1,1'-Dioctadecyl-3,3,3',3'-Tetramethylindocarbocyanine, 4-Chlorobenzene Sulfonate Salt (DiD, Invitrogen) before imaging, then washed twice with complete cell culture medium and injected intracardiac into the mouse at a concentration of 6 million per 300uL solution. To ensure that single cells were sequestered inside of blood vessels for single cell deformation studies, we tail vein injected a 50 µL volume of bovine FITC-albumin (5 mg/ml, ThermoFisher Scientific, A23015) approximately 10 minutes before intracardiac injection of single cells to label the blood vessel lumens.

Bacterial pneumonia model

We induced bacterial pneumonia in mice as previously described[66]. Briefly, *S. pneumoniae* serotype 3 (Sp3) (ATCC; Manassas, VA) was cultured on plates of BBL Trypticase Soy Agar with 5% sheep blood (BD Trypticase Soy Agar II) (BD Biosciences) in a 37°C humidified 5% CO2 environment for 10-11 hours and diluted in 0.9% sodium chloride to the desired optical density. Mice were anesthetized using a ketamine/xylazine cocktail (100 and 10 mg/kg, respectively) and approximately two million CFU in 50 µL were instilled into the left lung lobe via the left bronchus,

835 accessed through the surgically exposed trachea. Mice were sacrificed 24-36 hours post induction
836 to image the acutely injured lung.
837
838 **Pulmonary edema visualization**
839 Evans blue has historically been used as a label for vascular leakage and pulmonary edema in
840 rodent models of pulmonary disease as it binds serum albumin[67-69]. We injected 50 µl of 10 mg/ml
841 solution of Evans blue (ThermoFisher Scientific) with 100 µL of 1.25 mg/ml heparin saline into
842 the tail vein of mice 3-4 hours prior to excision of Sp3 infected lungs. Even after pulmonary
843 perfusion with unlabeled RPMI media, edematous regions of the lung retained the characteristic
844 blue color and far-red fluorescence of Evans blue (**Fig. 1e, Extended Data Fig. 9, Supplemental**
845 **Fig. 8**)
846
847 **Primary cancer model**
848 We induced tumorigenesis in 6-week female A/J mice as described previously[70]. Mice were treated
849 with a cocktail of Benzo[a]pyrene (BaP) (B1760, Millipore-Sigma, USA) (0.5 mg/dose) and 4-
850 (Methylnitrosoamino)-1-(3-pyridinyl)-1-butanone (NNK) (78013, Millipore-Sigma) (0.41
851 mg/dose) were dissolved in cotton oil (C7767, Millipore-Sigma) and delivered to the back of the
852 tongue using a metal 20G feeding tube, twice per week for 4 weeks and sacrificed at 20 weeks to
853 image the lung in the crystal ribcage.
854
855 **LPS acute inflammation model**
856 mTmG mice were treated with 100 µg *Escherichia coli* (*E. coli,* serotype O55:B5, Sigma-Aldrich)
857 lipopolysaccharide (LPS) diluted to 100 ug/60 µL in PBS via intratracheal injection using an
858 angio-catheter as previously described[71], to model acute injury. Mice were sacrificed 3-4 hours
859 post induction for microscopy of the acutely injured lung.
860
861 **Pulmonary fibrosis model**
862 Bleomycin was delivered to the lungs to generate a model of pulmonary fibrosis as previously
863 described[72]. Mice were anesthetized with ketamine/xylazine cocktail were given 1 U/Kg
864 bleomycin (APP Pharmaceutical, LCC Schaumburg, IL, USA) intratracheally using a 30G insulin
865 syringe. Mice were sacrificed 13-14 days after injection to image fibrotic regions. Collagen was
866 imaged using 2-photon second harmonic generated signal (SHG) and validated by Masson's
867 trichrome, and Col1A1 (E8F4L) XP Rabbit mAb cell signaling (Catalog 72026, ThermoFisher
868 Scientific) with Donkey anti-Rabbit IgG (H+L) highly cross-adsorbed secondary antibody alexa
869 fluor 555 (Catalog A-31572, ThermoFisher Scientific) staining of the same spatial locations
870 (**Supplemental Fig. 3)**
871
872 **Elastase induced emphysema model**
873 COPD was induced in mTmG mice by digesting the elastase in the lung using porcine pancreatic
874 elastase (PPE) (EC134 Elastin Product Company Inc., Owensville, MO). A previously published
875 protocol was followed for single dose treatment[73], briefly 6 IU PPE was dissolved in 100 µL saline
876 and delivered to the mouse (23-25 g). The solution was instilled at the back of the tongue of
877 anesthetized and vertically suspended mice, after which it was allowed to recover normally. Mice
878 were sacrificed at 21 days from instillation to image the lung inside the crystal ribcage.
879
880 **Histological staining for fibrosis evaluation**

881 Lungs were perfused with 10 mL of sterile cold PBS to remove blood then inflated with 4%
882 Paraformaldehyde (PFA). The trachea was clogged with a thread and lungs were fixed in 4% PFA
883 for 24 h at 24 °C. Fixed lungs were washed in 1x PBS three times 5 min at each interval at 24 °C.
884 Fixed lungs were dehydrated in 50%, 70%, 85%, 95% and 2x 100% ethanol, cleared in 3x Histo-
885 Clear (a xylene substitute, National Diagnostics) and embedded in paraffin. Formalin-fixed
886 paraffin-embedded (FFPE) tissues were cut to serial sections (5 µm). FFPE sections were
887 deparaffinized using a standard protocol of Histo-Clear and alcohol gradients. Masson's trichrome
888 staining was performed by using a commercially available kit (HT15-1KT, Sigma-Aldrich).
889 Hematoxylin and Eosin (H&E) staining was performed using Harris Hematoxylin solution
890 (ThermoFisher Scientific) and Eosin-Y solution (ThermoFisher Scientific). After dehydration in
891 70%, 95%, and 100% ethanol series and clearance with Histo-Clear, the stained slides were
892 mounted and imaged using Olympus BH-2 light microscope (Olympus).
893
894 **Immunofluorescence staining for fibrosis samples**
895 FFPE sections were deparaffinized using a standard protocol of Histo-Clear and alcohol gradients.
896 Antigen retrieval was performed by boiling the slides in citrate buffer (10 mM citric acid, 0.05%
897 Tween-20, pH 6.0) for 20 minutes, and then, the slides were allowed to cool at 24 °C for at least
898 30 min. The slides were washed with PBS and permeabilized with 0.2% Triton-X for 15 minutes.
899 Following blocking in 5% normal donkey serum in PBS containing 0.2% Triton-X for 2 hours at
900 24 °C. The slides were incubated with an antibody against COL1A1 (E8F4L rabbit mAb, 1:200,
901 Cell signaling Technology, #72026T) followed by a fluorescence-conjugated secondary antibody
902 (Donkey anti-Rabbit IgG (H+L) Highly Cross-adsorbed Secondary Antibody, Alexa Fluor 555,
903 ThermoFisher Scientific #A-31572, MA, USA, 1:1000 dilution) and DAPI (ThermoFisher
904 Scientific #62248, Waltham, MA, USA, 1:1000 dilution) to counterstain nuclei. Stained slides
905 were mounted with Aqua-Poly/Mount (Polysciences, Warrington, PA, USA) and imaged using
906 Olympus CKX53 inverted microscope (Olympus).
907
908 ***In situ* lung imaging**
909 Mice were anesthetized as described above and ventilated through a tracheal cannula to prevent
910 lung collapse before sacrificing the mouse. The skin and fascia were dissected the intercostal
911 muscles between the ribs was carefully separated under a stereomicroscope to expose the ribcage
912 pleura. A 2mm x 3mm retaining clamp was inserted in the cleared section to prevent the leftover
913 tissue strands blocking the opening. The PEEP on the lung was altered to confirm that the lung-
914 maintained contact with the internal pleural membrane and that the lung was responsive to pressure
915 changes. The mouse chest carcass was angled upwards for imaging.
916
917 **Lung preparation**
918 Isolated mouse lungs were ventilated (Kent Physiosuite Mouse ventilator, Kent Scientific) through
919 a tracheal cannula and perfused through two cannulas inserted into the pulmonary artery (PA) and
920 left atrium as previously described[44]. Perfusates included whole blood, cellular, or acellular media
921 containing fluorescent labels for vascular lumens and circulating cells. After cannulation, the lung-
922 heart bloc was placed into the crystal ribcage for microscopy under controlled
923 ventilation/circulation parameters. Perfusion pressure was controlled using a 60 mL reservoir
924 containing the perfusate medium (serum-free RPMI, Gibco) suspended at different hydrostatic
925 heights above the lung.
926

927
928 **Lung microscopy**
929 Prepared *ex vivo* lungs inside the crystal ribcage were imaged under quasi-static inflation
930 conditions or during dynamic ventilation using an inverted laser-scanning confocal microscope
931 (Olympus FV 3000) under objective magnifications of 1.25x, 10x, and 60x, with environmental
932 temperature control set to 37°C using FluoView (v2.5.1.228) acquisition software. The confocal
933 microscope was used with a resonant scanning mirror to increase the imaging speed up to 15 framer
934 per second (FPS) for imaging the dynamically ventilated lung, which increases speed by
935 compromising some of the image resolution. Additionally, lungs were imaged using an upright
936 Nikon fluorescent stereomicroscope, upright Nikon CSU X1 spinning disk confocal with 1x, 2x,
937 4x and 10x objectives, ThorLabs upright optical coherence tomography probe with a 10x objective
938 and an upright Bruker two-photon microscope (using Prairie View acquisition software) equipped
939 with a 16x water immersion objective. Microscopy data was visualized and processed using FIJI
940 and MATLAB R2021b, R2022a, R2022b.
941
942
943 **Crystal ribcage development and fabrication**
944 The entire development of the crystal ribcage is described as a supplemental protocol[74]. Briefly,
945 previously recorded µCT scans of C57B/6 and AJ mice chest cavities (courtesy the Hoffman group
946 at the University of Iowa[75-77]), and FVB mouse chest scans (performed at the Boston University
947 Micro-CT imaging facility) were segmented in MATLAB (R2019b Mathworks, Natick MA) and
948 imported into Solidworks 2019 (Dassault systems, France) to create a refined geometry of the
949 chest.The model was made age-specific by scaling the binary object by mouse lung volume
950 reported by age[78] (**Extended Data Fig. 1**) and printed in FormLabs (Somerville, MA) clear resin
951 on a Form3 printer. The mold was polished to get a high gloss surface finished buck. A sacrificial
952 sugar mold was cast from the buck to make semi-flexible polymethyldisiloxane (PDMS) ribcage.
953 The buck was used directly to thermoform polystyrene sheets over it to make the rigid crystal
954 ribcage. The internal surface of the PDMS crystal ribcage was treated with a 1% PDMS-PEG
955 Block Copolymer (DBE-712, Gelest Inc., Morrisville, PA) and allowed to cure to improve
956 hydrophilicity as previously described [79].The rigid crystal ribcage was treated in an oxygen plasma
957 cleaner to make the surface hydrophilic.
958
959 **Quasi-static alveolar diameter measurement**
960 Microscopy images recorded with a 10x objective and an additional 1.5x optical zoom were loaded
961 into FIJI-ImageJ and sum-wise projected in the z-direction for all pressure conditions. Alveoli
962 common to all quasi-static or dynamic pressures were annotated prior to making measurements.
963 The mean alveolar diameter was calculated by recording 2 length values between anatomical
964 features that were diametrically opposite to each other. The mean lengths were recorded for all
965 corresponding alveoli at different pressures. These measurements were compiled in MATLAB
966 R2021b to make raincloud plots[80] and compute group-wise statistics.
967
968 **Alveolar septum strain calculation**
969 We used a previously published deformable registration algorithm, deedsBCV[81] to autonomously
970 determine the displacement map between images of the lung tissue at different quasi-static
971 inflation pressures, here alveolar pressures of 7 and 12 cmH_2O. We subsequently used a custom
972 algorithm (finite difference methods are subject to noise that obscures signal) to compute the strain

973 map (**Supplemental Fig. 6**) with a cubic smoothing spline to approximate the displacement map
974 and evaluate its gradient derivative and calculate the canonical strain tensor components directly.
975 This method gives us a displacement gradient continuous in its second derivatives which avoids
976 obscuring the true signal in the noise. We validated the obtained displacement maps against known
977 displacements applied to images being registered. We validated the effect of the smoothing spline
978 with multiple kernel sizes to ensure that the final registered image matches the target image. The
979 final strain computation algorithm was validated for known synthetic displacement maps to ensure
980 parity between the mathematical ground truth and image-based strain estimation.
981
982 **Dynamic alveolar diameter measurement**
983 The 2-D image series of the lung were loaded in MATLAB R2022a and segmented by applying a
984 global threshold to each image. The binarized images were analyzed using the built-in *regionprops*
985 function to obtain the equivalent diameter of a circle with the same area as each binarized segment.
986 Diameters greater than 500 μm or less than 10 μm were ignored. The mean diameter of each image
987 was plotted as a time series and the peaks of the curve were obtained to find when the cycle was
988 repeated. The total number of frames were linearly distributed to obtain a normalized ventilation
989 cycle and pooled to get a single mean alveolar diameter curve per ROI to obtain the width at half-
990 maximum of the ventilation cycle for each ventilation rate.
991
992 **Collagen waviness quantification**
993 The 3-D images of the tumor nodules were imaged with a Bruker 2-photon microscope with the
994 laser excitation set at 920 nm. The dendra signal from cancer cells was collected through a 525/50
995 nm emission filter and the second harmonic generation collagen signal was collected through a
996 460/50 nm emission filter on separate channels. The speckle noise was removed from the 3-D
997 stack using a 2-pixel median filter in MATLAB R2021b medfilt2() and manual traces were made
998 along the collagen fibers between successive nodes. The total path length traced was divided by
999 the end-end distance of the start and end points of the trace to determine the waviness index.
1000
1001 **Single cell measurement**
1002 Microscopy images at each quasi-static pressure condition were loaded into FIJI-ImageJ and cells
1003 were traced around manually. Circularity of single cancer cells was calculated as $4\pi \frac{area}{perimeter^2}$
1004 The tabulated results were compiled in MATLAB R2021b to perform statistical comparisons
1005 between the groups of cells at each condition. We confirmed that single cells were sequestered
1006 inside blood vessels by exclusion of FITC-albumin dye, which was injected into the mouse via the
1007 tail vein (50 μL of 10 mg/ml FITC-albumin in saline) prior to injection of singularized cancer
1008 cells.
1009
1010 **Cancer nodule size estimation**
1011 We estimated the size of cancer nodules for the analysis reported in **Fig. 2h** by first assuming an
1012 average cell size of 10 μm and measuring the diameter of the cancer nodule in in the XY plane,
1013 from confocal microscopy images of nodule-bearing lungs in the crystal ribcage from confocal
1014 microscopy images (representative image in **Fig. 2a**). We estimated the size of the nodules in terms
1015 of cell number by dividing the diameter of the nodule by average cell size.
1016
1017
1018 **Perfusion and vascular transport data analysis**

1019 We extracted the mean fluorescent intensity across all pixels in the perfusion timelapse video, at
1020 each time frame for each ROI. Then, we normalized the mean fluorescent intensity curve of each
1021 ROI to the maximum of the mean intensity from all ROIs. Multiple replicates for each ROI are
1022 combined to produce a final normalized mean intensity (solid line) and the respective standard
1023 error of the mean (shaded areas). The duration of dye intensity greater than 50% of the normalized
1024 maximum intensity was reported as T_{50}. The time from initial increase in pixel intensity time series
1025 to the normalized maximum intensity was calculated (T_{max}). Step bolus injections for tumor
1026 diffusion were processed in ImageJ to obtain dye intensity intratumor and normalized to baseline
1027 intensity measured within the vasculature.
1028
1029 **Cell tracking for neutrophil migration**
1030 Post-processing of neutrophil migration data was performed in MATLAB2021b. Multi-channel
1031 recordings from microscopy were stabilized and single neutrophil centroids were computed per
1032 frame to obtain corresponding position and speed information. Persistence was calculated as the
1033 total displacement divided by contour length of the path. Where relevant, migration through the
1034 intravascular space was defined as movement confined within the vasculature, intra-alveolar as
1035 movement within alveolar spaces, and interstitial as those crossing between vascular and alveolar
1036 spaces. Neutrophil shape was segmented using an intensity threshold and the *regionprops* function
1037 was used to compute aspect ratio and circularity.
1038
1039 **Statistics and Reproducibility**
1040 No statistical method was used to predetermine sample size and no data were excluded from the
1041 analyses. The experiments were not randomized, and investigators were not blinded to allocation
1042 during experiments and outcome assessment. All experiments were performed at least twice in
1043 separate mice to generate biologically independent samples. Data are presented as mean ± standard
1044 error of the mean (SEM). All statistics presented here were calculated as a two-tailed Student's t-
1045 test to determine significance or p-values between groups of data. All p-values are reported on
1046 figures for the users to observe statistical trends of data. Significant differences were considered
1047 when $p < 0.05$. Statistical analyses were performed in MATLAB R2021b and R2022b.
1048
1049

Data Availability: A demonstration data set has been deposited in a Zenodo repository[82] and are available from DOI: doi.org/10.5281/zenodo.7939072. Additional microscopy data is available on request from the corresponding author.

Code availability: The source code and algorithms used in this study have been deposited in a Zenodo repository[82] and are available from DOI: doi.org/10.5281/zenodo.7939072 licensed under the CC BY 4.0 for use in research.

Extended Data Figures

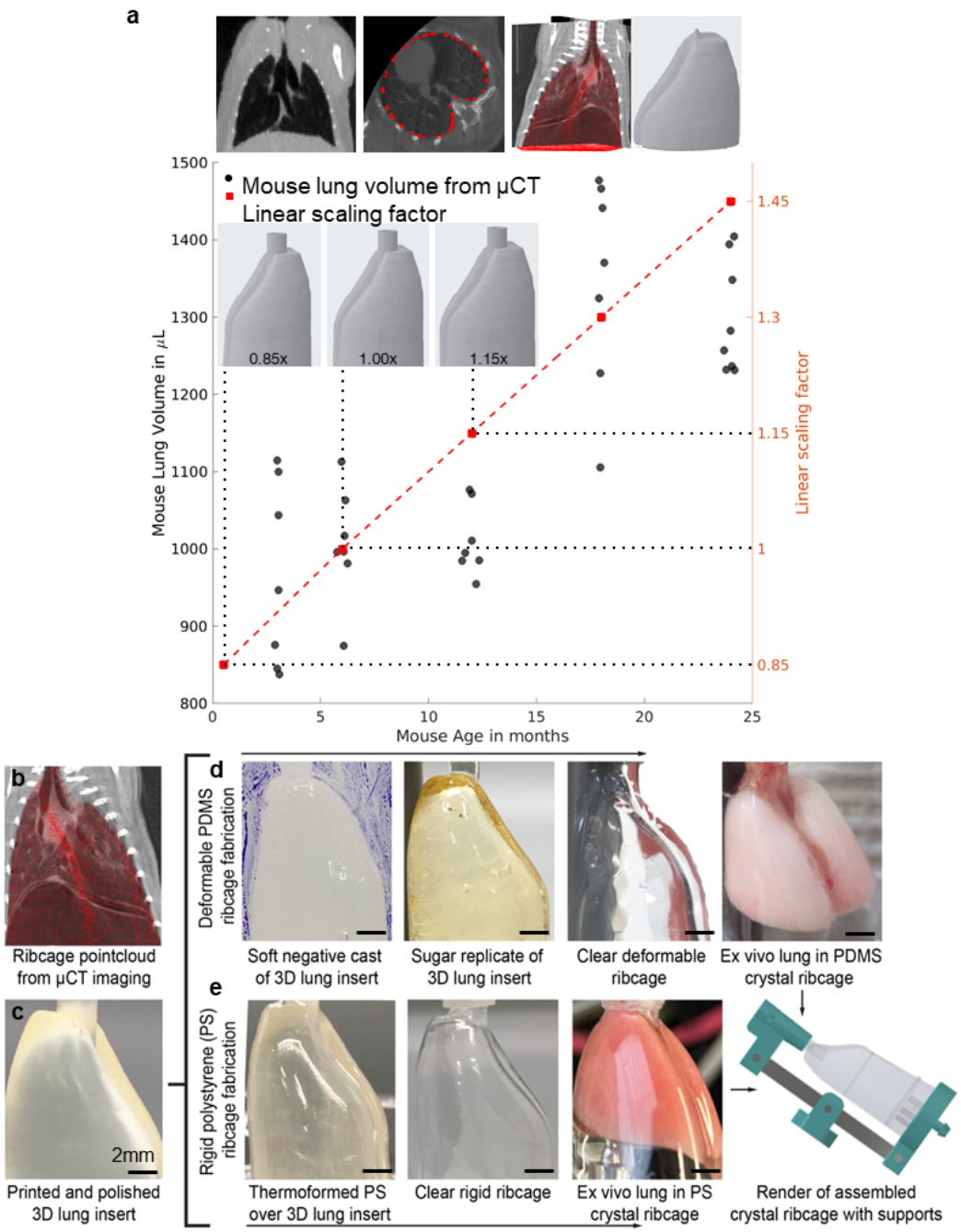

Extended Data Figure 1 | Mouse strain specific µCT informed 3D molds scaled by age and fabrication of crystal ribcages. (a) Recreating mouse ribcage geometry from µCT data[75-77], here shown for C57/B6 mice. Top: Sagittal view of mouse chest with fully inflated lung (dark region), distribution of axial control points to recapitulate ribcage cross-section and comparison of reconstructed geometry overlaid on sagittal and coronal µCT slices. Lung volume variation[78] with age was normalized against the mean volume at 3 months to construct a linear fit for scaling 3D lung inserts by age. (**b-e**) 3D printed models were used to make both PDMS and polystyrene crystal ribcages in two independent processes[74].

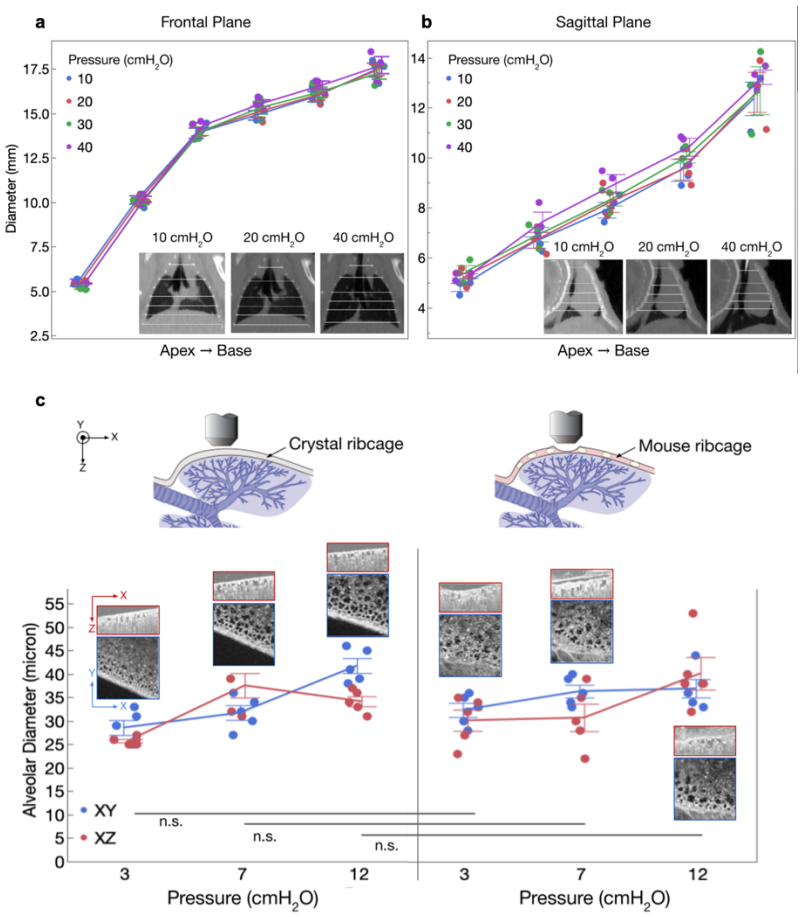

Alveolar behaviour across pressures is maintained in the crystal ribcage as in the mouse ribcage

Extended Data Figure 2 | Native mouse ribcage does not show significant variation in diameter across its anatomy and alveolar function (diameter in µm) remains unchanged between crystal ribcage and mouse ribcage. Previous µCT data[75-77] used to define the mouse chest cavity was also used to (**a**) quantify the expansion of the native mouse ribcage as a function of pressure and anatomical location during *in situ* ventilation. There was no significant difference between the ribcage diameter at tracheal pressures ranging from 10 to 40 cmH_2O in both the frontal and sagittal planes from the apex to the base of the ribcage. The increase in volume with increasing pressure was accommodated by the increasing length of the lung (movement of diaphragm and abdomen) and not the width of the ribcage. This confirms that there was little contribution of the changing ribcage diameter to lung volume change during normal physiological conditions *in situ*. The scatter of the data over n=3 mice is presented along with the mean ± SEM traces. (**b**) A mouse ribcage was thinned down to make a window above the pleural sheath to image the functional lung using OCT, the same lung was then measured in the crystal ribcage for the same changes in pressure. There was no significant difference between alveoli function (measured as changing diameter) across the pressure range for m=5 ROI over n=1 mouse. The scatter of the data is presented along with the mean ± SEM traces. Comparison between groups performed with two-tailed Student's t-test for significance < 0.05.

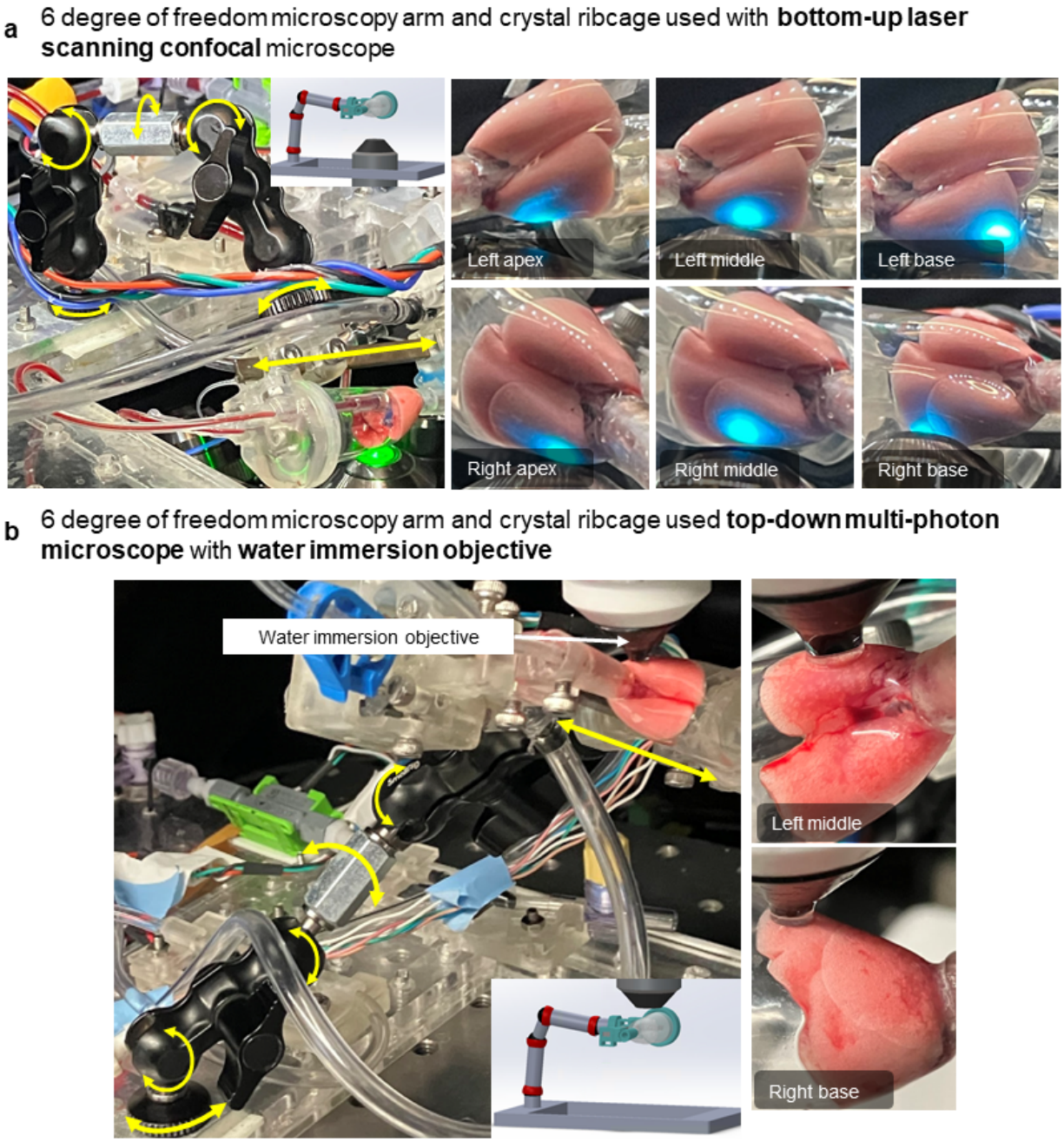

Extended Data Figure 3 | Experimental setup and 3D renders of the microscopy arms used to image different orientations of the crystal ribcage with upright and inverted microscope configurations. We successfully used the stage to image (**a**) with an inverted Olympus Fluoview 3000 laser scanning confocal microscope and (**b**) with upright microscopes, such as the ThorLabs optical coherence tomography probe and Bruker multi-photon microscope. The crystal ribcage is microscope agnostic and compatible with both air and water-immersion objective in both configurations.

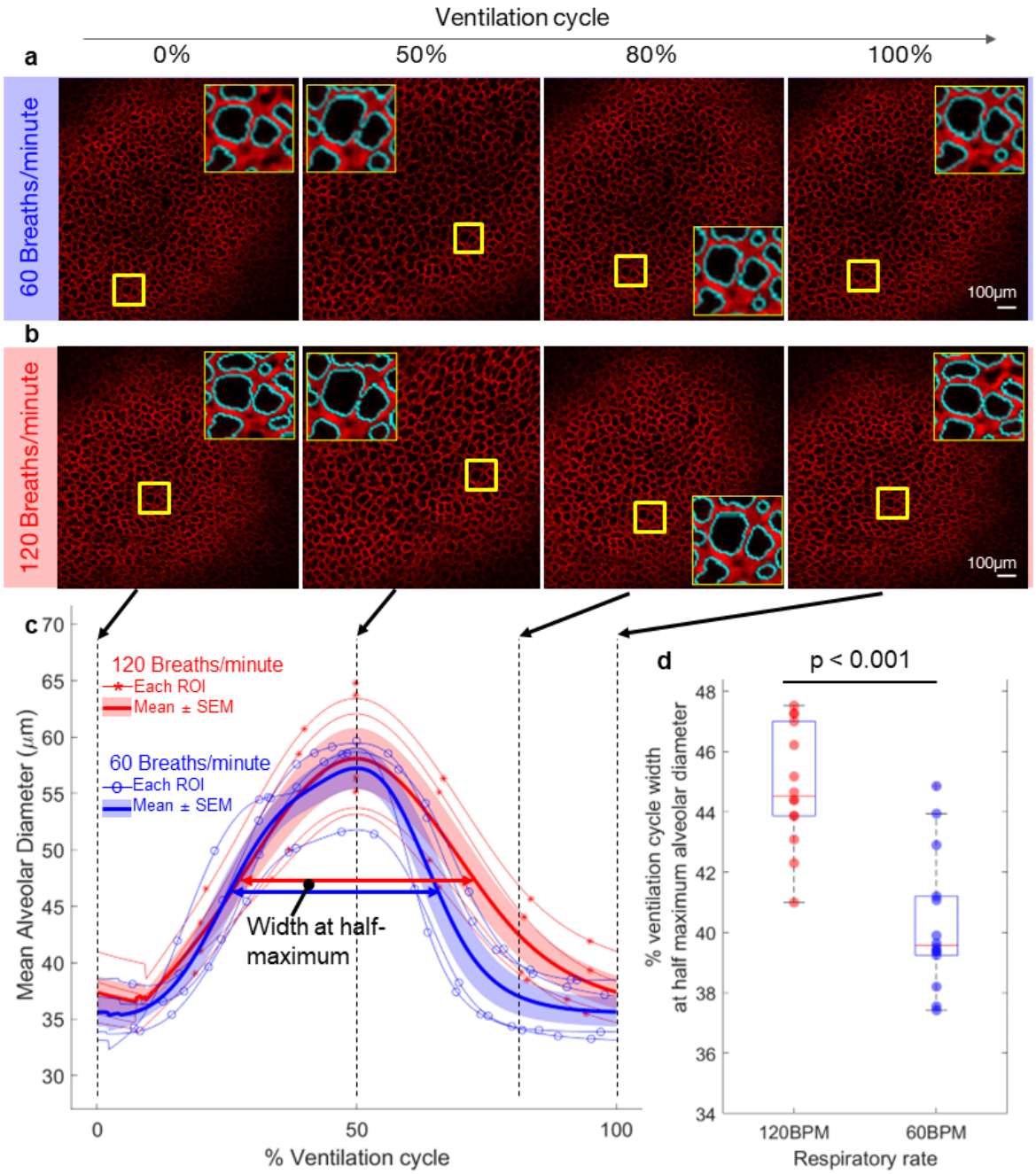

Extended Data Figure 4 | Dynamic ventilation of mouse lung shows alveoli remain at a larger diameter for longer duration at higher ventilation rate. Comparing the same region of the lungs ventilated at (**a**) 60 breaths/minute with (**b**) 120 breaths/minute by (**c**) the mean ± SEM alveolar diameter from m=4 ROI over n=2 mice with a normalized ventilation cycle. Blue traces in the inset images show the segmentation boundary drawn to quantify single alveoli. (**d**) The width of the normalized ventilation cycle from m=4 ROI over n=2 mice at each respiratory rate are statistically larger at the higher respiratory rate. Boxplots present median with 25th and 75th percentiles, whiskers are the maximum and minimum data points not considered outliers. Comparison between groups performed with two-tailed Student's t-test for significance < 0.05.

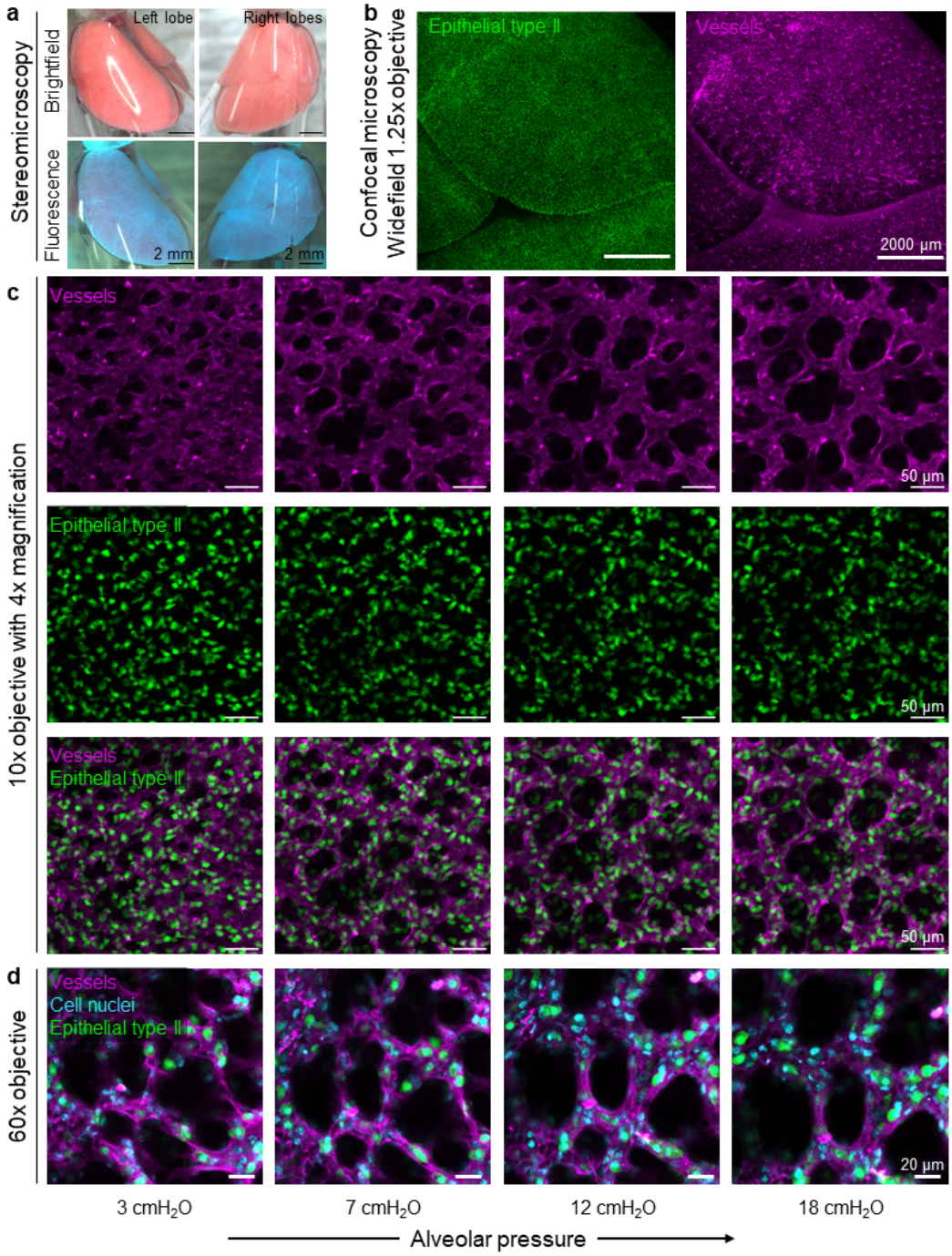

Extended Data Figure 5 | Resident alveolar type II cells, with GFP-labelled surfactant protein C (green) can be imaged inside the crystal ribcage. (**a**) Stereomicroscope fitted with a NightSea GFP filter to visualize the SPC-GFP distribution at the whole organ scale. (**b**) Confocal microscopy of the SPC-GFP population at the lobe scale on the right side of the lung at 1.25x magnification. Vessels are labeled by injection of 50 µL of 10 mg/ml Evans blue dye in saline *in vivo* prior to extraction of the lungs. (**c**) Confocal microscopy at the 10x magnification shows single SPC-GFP+ cells in the lung distal parenchyma. (**d**) Single cell nuclei and SPC-GFP signal in cell cytoplasm visible at single cell resolution using a 60x water immersion lens.

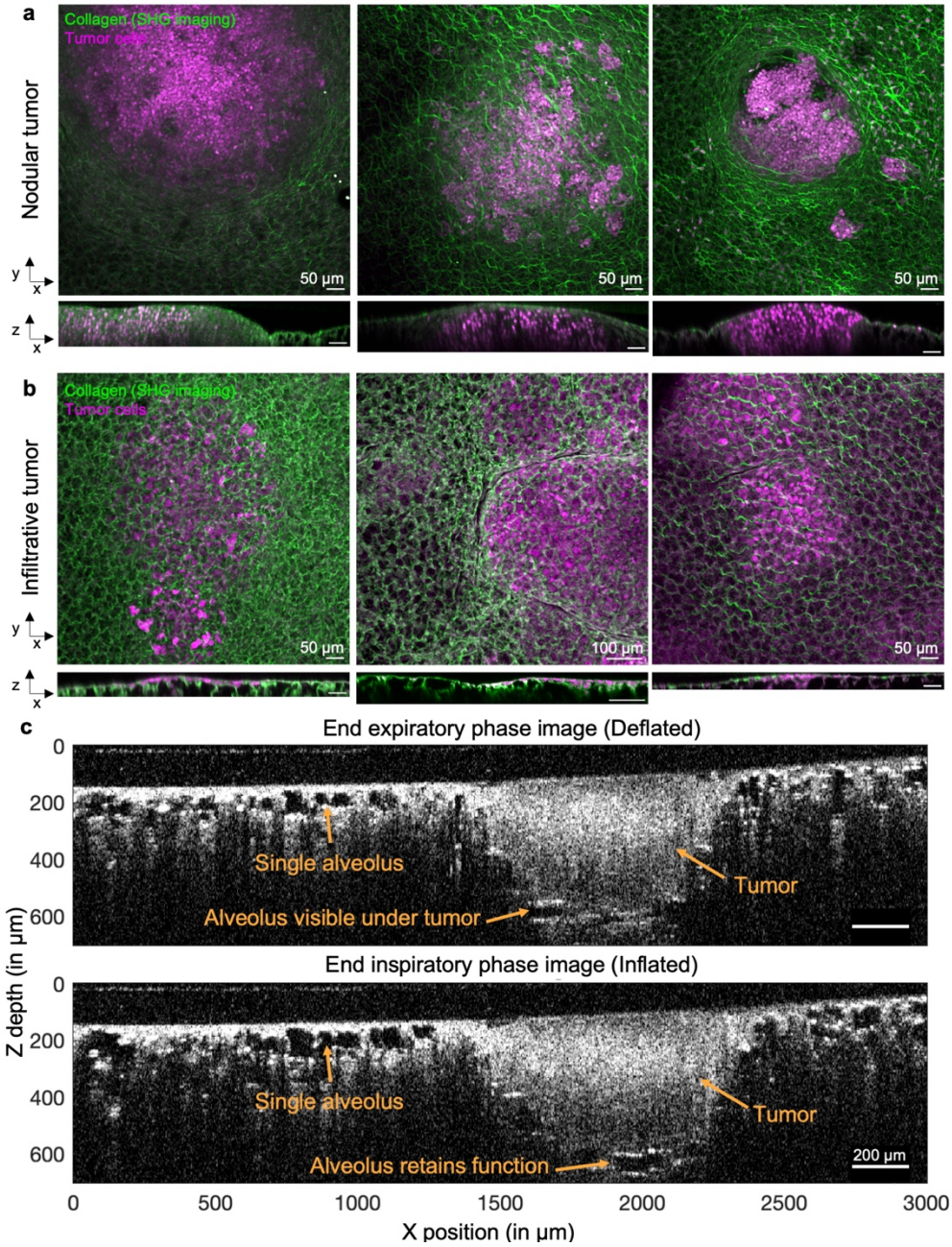

Extended Data Figure 6 | Orthogonal views comparing the spatial distribution of nodular and infiltrative tumors, for three separate instances of each phenotype and solid phase nodular growth tumor increases imaging depth in sagittal image section using optical coherence tomography. (**a**) Nodular tumors extended into the lung tissue to greater depths and bulge out of the pleural surface. (**b**) Infiltrative tumors are located more superficially on the pleural surface. (**c**) Alveolar function deeper than 100µm from the surface can be imaged through the tumor nodule up to a depth of 400µm from the surface, as the gas phase of the alveoli is replaced by the solid phase tumor, which reduces light scattering.

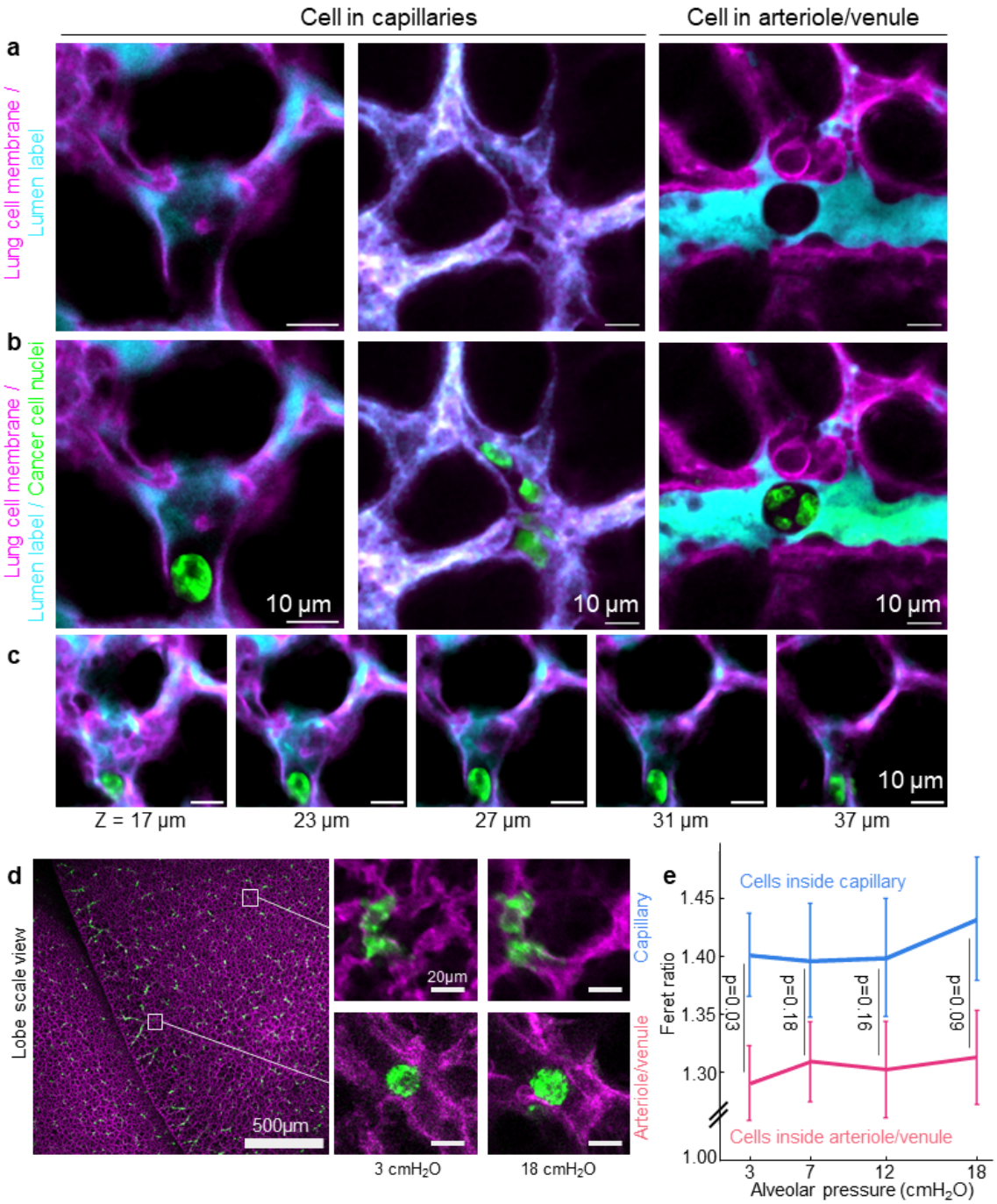

Extended Data Figure 7 | Single cell deformation in response to changing alveolar pressure. (**a**) Cell-scale confocal microscopy of the lung inside the crystal ribcage with a FITC-albumin vascular lumen label showed the shadow of the cancer cell (**b**) which was imaged in a separate channel and merged to show cancer cells stretched in capillaries compared to arterioles and venules. (**c**) XY- views of the cancer cell at different depths of confocal imaging to show the cell is completely enclosed in the capillary. (**d, e**) Cells in capillaries quantified by the Feret ratio trended towards greater deformation in comparison to cells in larger arterioles-venules. Feret ratio quantified for n=40 cells in capillaries, n=30 cells in arteriole-venule at each alveolar pressure and data presented as mean ± S.E.M.

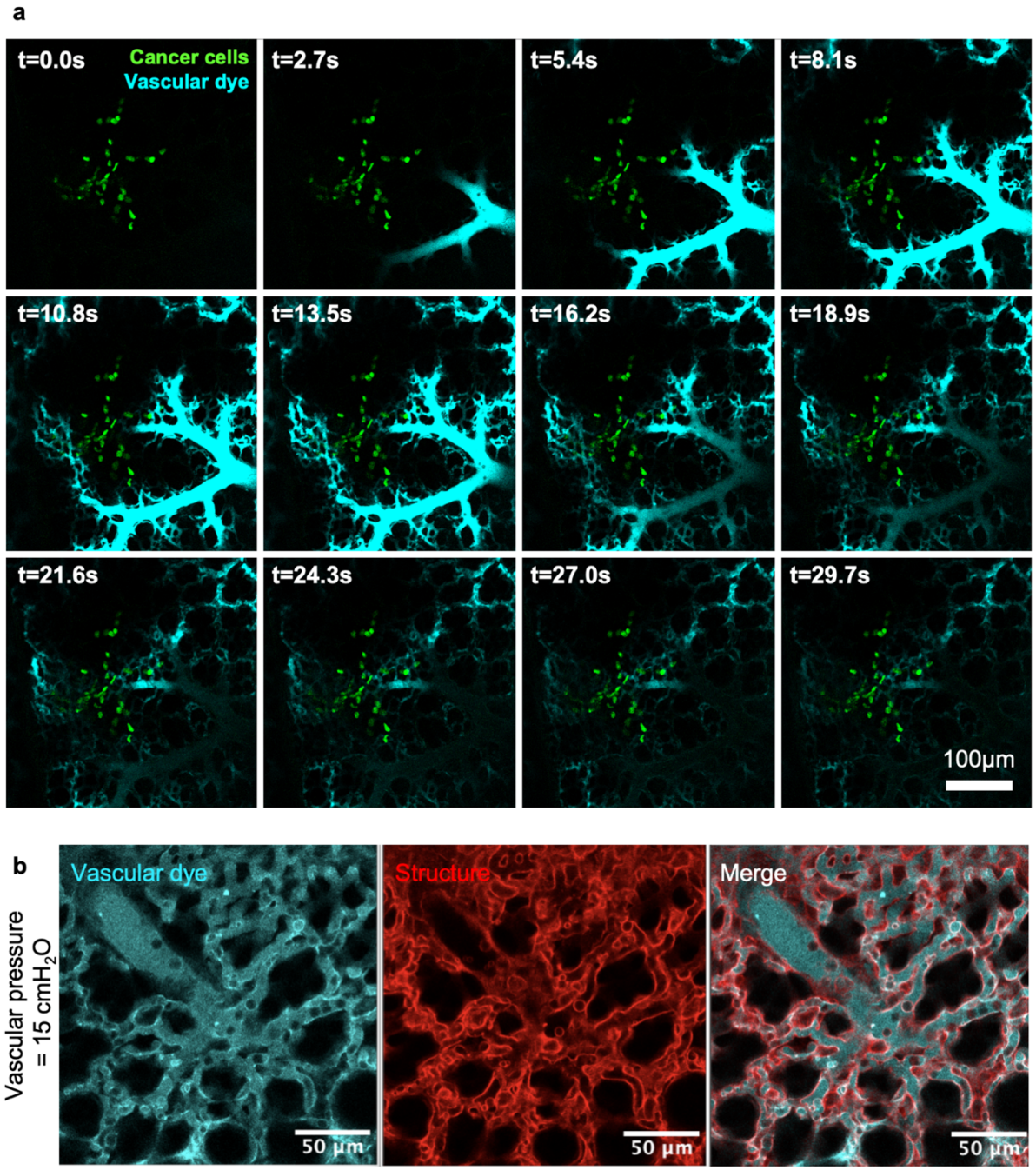

Extended Data Figure 8 | Metastatic cancer cells disrupt vascular dye distribution in capillaries and the crystal ribcage used to visualize individual lung capillary walls and perfused lumens at high magnification (60x). (**a**) Capillary scale confocal microscopy imaging of single cancer cells that disrupt the distribution of dye observed over a time lapse imaging. (**b**) Vascular lumens were labeled with 10 mg/ml FITC-albumin dissolved in saline, injected intravenous prior to excision of the lungs for high-resolution confocal microscopy with a 60x objective.

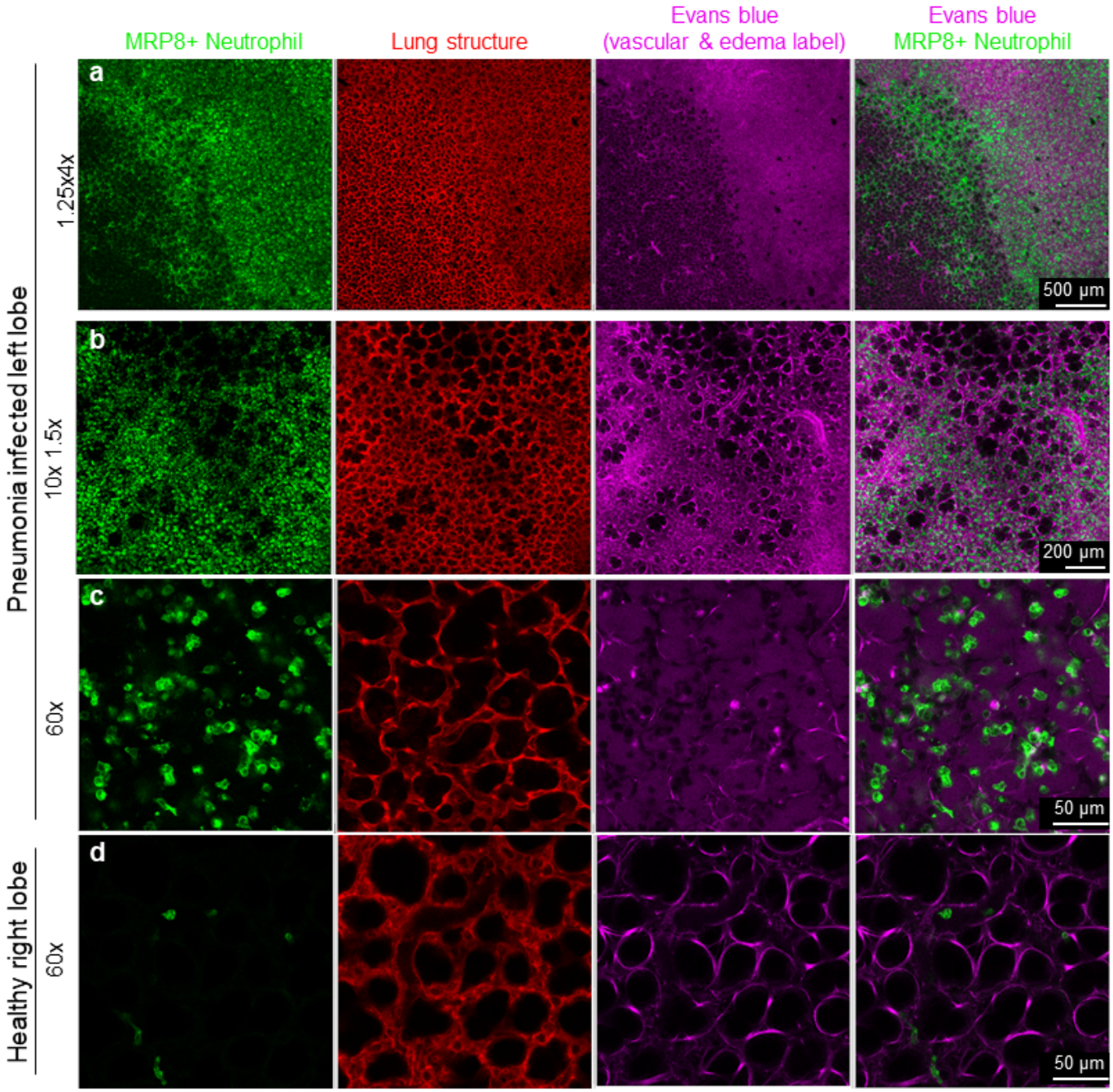

Extended Data Figure 9 | MRP8+ Neutrophil cells co-localized with edema in lungs after at 30 hours lobar pneumonia injury. Correlation of the edema label with neutrophil cells is imaged (**a**) using 1.25x, (**b**) 10x and (**c**) 60x objectives to confirm that all alveoli with neutrophils (green) are edematous (magenta). (**d**) The contralateral lobe was also imaged to show the absence of edema and neutrophils inside alveoli.

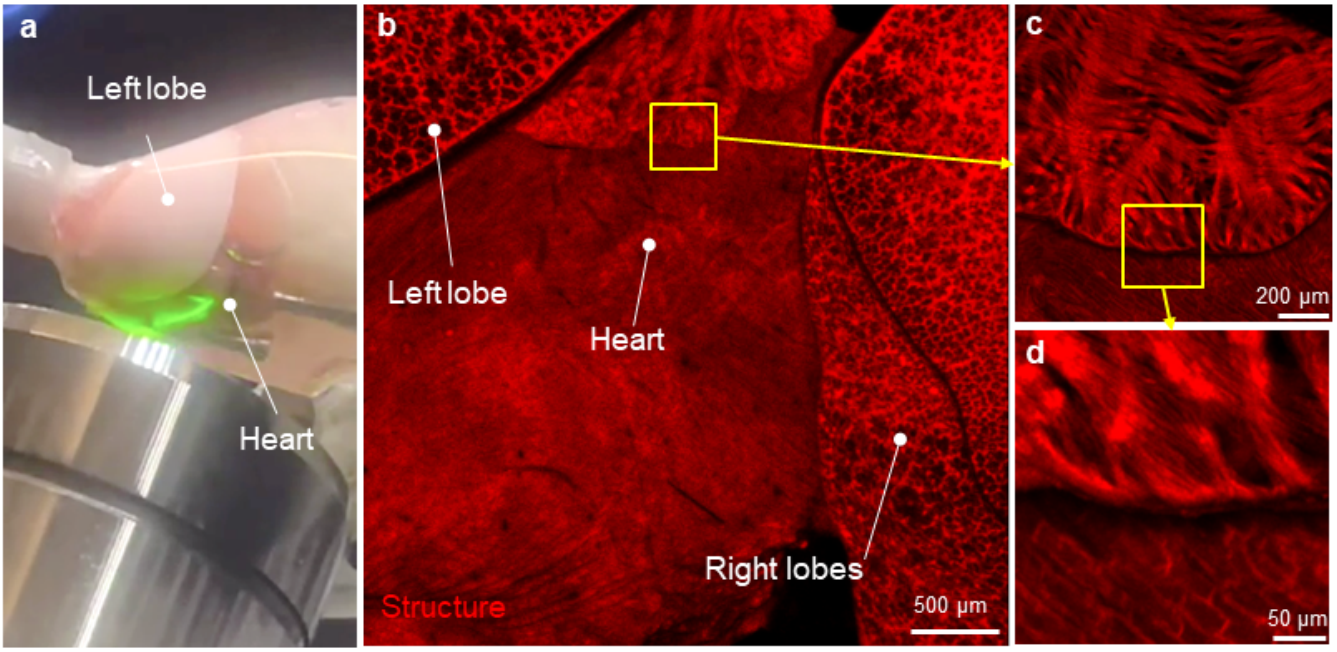

Extended Data Figure 10 | Lung adjacent organs such as the heart can also be imaged with the crystal ribcage. Here using a laser scanning confocal (**a**) the heart is imaged with a 1.25x objective to show (**b**) the overlapping lobes of the lung followed by (**c**) higher resolution images of the atrial surface and (**d**) muscle structures.